

# Photon-Enhanced Thermionic Emission

## Final report

**Authors:** W. Raja<sup>1</sup>, P. Zilio<sup>1</sup>, A. Alabastri<sup>1</sup>, R. Proietti Zaccaria<sup>1</sup>, J. Cunha<sup>2</sup>, L. Summerer<sup>2</sup>, T.W. Versloot<sup>2</sup>

**Affiliation:**

<sup>1</sup>Instituto Italiano di Tecnologia (IIT),

<sup>2</sup>Advanced Concepts Team, European Space Agency (ESA)

**Date:** 05/10/2015

**Contacts:**

Remo Proietti Zaccaria

Tel: +39 010 71781247

Fax: +39 010 720321

e-mail: remo.proietti@iit.it

Leopold Summerer (Technical Officer)

Tel: +31(0)715654192

Fax: +31(0)715658018

e-mail: act@esa.int



Available on the ACT website  
<http://www.esa.int/act>

**Ariadna ID:** 14/2101b  
**Ariadna study type:** Standard  
**Contract Number:** 4000112048/14/NL/MV

# Space Charge Theory for Photon Enhanced Thermionic Emission in space oriented applications

## 1. Introduction

Photovoltaic (PV) solar cells and thermionic energy converters (TECs) are among the main technologies, suitable for space applications, addressing the issue of electricity generation [1,2]. The interest in these technologies by space agencies rely on the requirement for high-power and long-life generators which can be exploited during deep-space or near sun missions. In a PV cell, solar photons with energy comparable or above the band gap of a semiconductor, excite the electrons from the valence to the conduction band. These excited electrons can then be fed into an external circuit to generate electrical power. Recent reduction in manufacturing cost of silicon based solar cell technology has resulted into an extensive use of photovoltaics for electricity generation [3]. However, non-renewable resources such as coal produce almost 40% of global electric power. This limitation in PV technology is due to its low power conversion efficiency. In particular, in standard solar cells, about 50% of the total incident solar radiation is lost due to thermalisation losses and a further 25% is not transformed in electrical power because the corresponding photons do not carry enough energy with respect to the semiconductor band gap (absorption losses). Furthermore, when thin film solar cells are considered, the lost power can be even higher than 50% as shown in Fig. 1 for a 300nm thick a-Si solar cell.

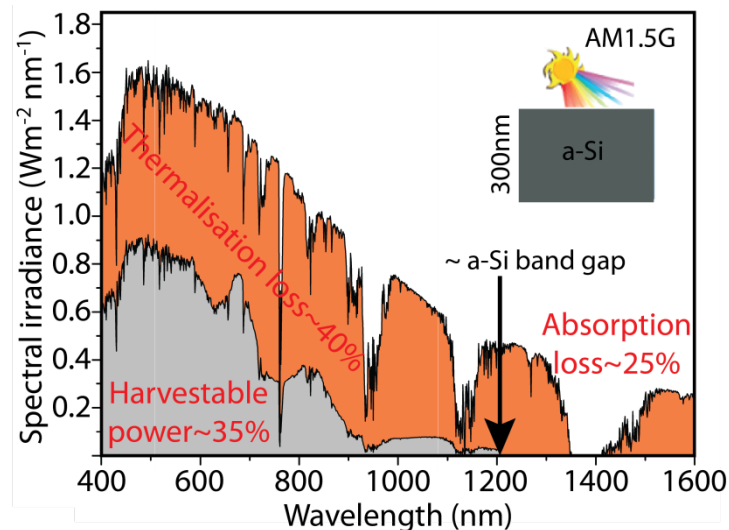


FIG. 1 AM 1.5G spectrum showing the fraction of incident radiation (highlighted in gray) absorbed by a 300 nm a-Si thin film solar cell together with the spectral region that cannot be utilized due to either thermalisation or absorption loss (highlighted in orange).

On the other hand, TECs technology follows a complementary approach to PV, being based on the heat-to-electrical current transformation principle [4]. It involves the emission of electrons through an heated metal electrode (cathode) in a vacuum chamber and their collection on a cooler metal electrode (anode), resulting in a net electron flow from the cathode to the anode (inter-electrode space). In 1885, W.H. Preece [5] first reported about this phenomenon, known as thermionic emission. Later on W. Schlichter [6] in 1915 published the idea which describes the conversion of heat to electricity and after that the subject went through an intensive research from 1950s to 1960s [7,8]. In 1980s, space agencies and research institute such as National Aeronautics and Space Administration (NASA), the Department of Energy (DOE) and the Defence Advanced Research Projects Agency (DARPA) established a collaborative project to study and implement thermionic emission devices for space applications making TICs the primary power sources for space missions [9]. Despite its great potential, the further development of TECs has been held back due to their low power

conversion efficiency. There are mainly two drawbacks of TECs: i) there is the strict requirement of long time thermal stability, as the operating temperature is above 1000 °C, and the need of low emitter and collector work functions in order to achieve the maximum conversion efficiency. In this regard, it has been reported that Cs based coatings can lower the work function of electrodes [10]; ii) the space charge (SC) cloud represents an important issue needed to be solved. In fact, the electron cloud within the inter-electrode space tends to drastically reduce the current density, in turn the output power and the efficiency of the device. Three schemes have been developed and implemented both theoretically and experimentally to reduce the SC potential. First, decreasing the emitter-collector distance leads to fewer electrons in the intermediate space between cathode and anode which results into faster collection of electrons at the anode side. However, it is reported that for practical devices, due to the close-space proximities between the emitter and collector, a decline in the device performance can occur due to the difficulty in controlling and maintaining very small distances between emitter and collector under high temperature condition [11]. Furthermore, recent studies show that with a gap size below 1  $\mu\text{m}$ , additional processes such as electron tunnelling or increased parasitic losses due to near-field radiative heat loss come into play with detrimental effects on the efficiency of the device [12,13]. Second, positively charged ions are inserted into the vacuum space in order to counterbalance the negatively charged space cloud. The downside of this process are energy losses through electron collisions and additional heat transfer through the inserted gas [14]. Third, an electric field produced by a gate electrode inserted in the vacuum space can be used to accelerate electrons away from the emitter surface, as the SC cloud becomes weaker due to the higher velocity of electrons. This turns into a significant enhancement in collection of electrons at the collector. In this regard, S. Meir et al. [15] have demonstrated that the insertion of a positively charged gate electrode into the inter-electrode space can compel electrons to accelerate away from the cathode, thus reducing the SC accumulation, thereby resulting in enhancement of net current derived from TECs. S. Meir et al. [14] and C. Stephanos et al. [11] provide an extensive overview in their thesis about the influence of SC cloud and enhancement in power conversion efficiency through gate insertion. They also put forward some preliminary results about remedial solutions of the SC problem by gate terminal insertion, to improve the power conversion efficiency of TECs devices. Both NASA and the Soviet space programme funded the development of TECs for space missions but it was never commercialised due to the high temperature requirements and intrinsic losses due to the SC problem [16].

Photon-enhanced thermionic emission (PETE) combines the quantum and thermal processes obtained respectively from photovoltaics and TECs into a single physical process to take simultaneously advantage of absorbed photons and of the available thermal energy of the incoming light. In a PETE device, using a semiconductor as a cathode, incoming photons with energy above its band gap can promote valence electrons into the conduction band, setting them closer to the vacuum energy of the material. After thermalisation these electrons will need a relatively lower energy, namely lower temperature, to overcome the cathode work-function with respect to valence electrons. In this way the solar flux exploitation is optimized: on the one hand the photons quantum energy is utilized to promote electrons above the band gap, on the other hand the sub-band gap photons and the thermalized electrons in the conduction band contribute to increase the cathode temperature. Schwede et al. [17] first proposed the idea of PETE device and predicted that, by exploiting the contribution of both thermal and photovoltaic processes together, the device could surpass the Shockley Queisser limit for single junction solar cells, theoretically reaching the power conversion efficiency of 50%. Since then, several reports have been presented both theoretically and experimentally claiming that PETE could be the solution for low efficiency devices, both single and multijunction solar cells, and entered in the category of third generation solar cell [18–21]. Recently, G. Segev et al. [18] reported that the waste heat removed from the anode can again couple into the device which goes through the heat-to-electricity conversion stage, and theoretically enhances the PETE device power conversion efficiency up to 70%. In a PETE device, electrons emitted from the cathode require a finite amount of time to reach at anode. Similarly to TECs, the negatively charge cloud in between the inter-electrode space drastically reduces the current density, the output power and the efficiency of the device. S. Su et al. [23] recently published the analysis of SC effects on the

efficiency of a PETE converter through Langmuir SC theory, which was originally proposed for TECs [24]. Likewise TECs, other methods have been proposed to reduce the SC effect in PETE device. T. Ito et al. [25] demonstrated that adding caesium ions into the vacuum space could reduce the SC barrier. Furthermore, it has been also verified that by reducing the distance between cathode and anode the SC cloud is reduced as well [26]. S. Su et al. [23] were the first to investigate the effect of SC cloud on the performance of PETE, particularly its power conversion efficiency. Furthermore, G. Segev et al. [26] published an article claiming that in PETE device the electrons which are reflected back by the SC can be absorbed by the cathode to be reemitted back into the inter-electrode space forming a sort of recycling effect which improves the PETE performance.

All considering, when it comes to spatial applications they still rely mostly on conventional photovoltaic systems which have the drawback of losing performance when operating above a maximum steady-state temperatures [22]. This implies an urgent need for power conversion devices enabling operation at elevated temperatures, making PETE a promising technology especially for near-the-Sun missions as PETE can operate in the temperature range of 673-1300 K [17].

In this work, we shall start by using the Langmuir theory to investigate the influence of SC on the net current density which directly relates into power conversion efficiency for one dimensional (1D) TECs. Furthermore, we will use the same theory to investigate the SC effect in 1D PETE device. This can be done by solving the self-consistent Poisson's equation which gives us the information of electrostatic potential formed within the inter-electrode space. The obtained potential is used to determine the electrons trajectories in the inter-electrode space under the influence of the SC potential. The next step is to move towards the 3D modelling [28] inasmuch as the Langmuir SC theory is limited to 1D and 2D [27] investigations. Hence, we implemented a 3D Finite Elements Model for investigating the SC potential influence on the net current flowing within the device. Furthermore, we inserted a gate terminal into the inter-electrode space to minimize the SC screening effect. Finally, to test the capabilities of the simulation setup to model the SC problem in complex 3D structures, we considered a nanostructured cathode given by an array of nanocones with variable apex radius.

## 2. One Dimensional (1D) space charge Langmuir Theory for TECs

To derive the inter-electrode electrostatic space charge potential  $\Phi_{sc}(x)$  caused by the electron cloud, we follow the analytical expression of differential equation derived by Langmuir [24] and G. Hatsopoulos et al. [29] which can be expressed through the Poisson's equation:

$$\Delta\Phi_{sc}(x) = -\frac{\rho_{sc}(x)}{\epsilon_0} \quad (1)$$

Where  $\rho(x)$  is the SC density within the inter-electrode space and  $\epsilon_0$  is the free space permittivity. To solve Eq. 1, G. Hatsopoulos et al. [29] expressed the SC density  $\rho_{sc}(x)$  in terms of the space charge potential  $\Phi_{sc}$ :

$$\rho_{sc}(x) = 2qn_0 \left( \frac{m_e}{2\pi k_B T} \right)^{\frac{1}{2}} \int dv_x e^{-\frac{q\Phi_{sc}(x)}{k_B T} - \frac{v_x^2}{k_B T}} \quad (2)$$

Where  $n_0$  is the number of electrons for unit volume,  $m_e$  is the electron mass,  $q$  is the electron charge,  $k_B$  is the Boltzmann constant and  $T$  is the operating temperature at the emitter side,  $v_x$  is the velocity distribution along the x direction of the vacuum gap of TEC (see Fig. 2.1). As the Poisson's equation indicates, considering fixed  $\Phi_{sc}$  at the emitter and the collector surface, the  $\Phi_{sc}(x)$  profile always forms a maximum at  $x=x_{max}$ , as shown by the charge distribution in Fig. 2.1.

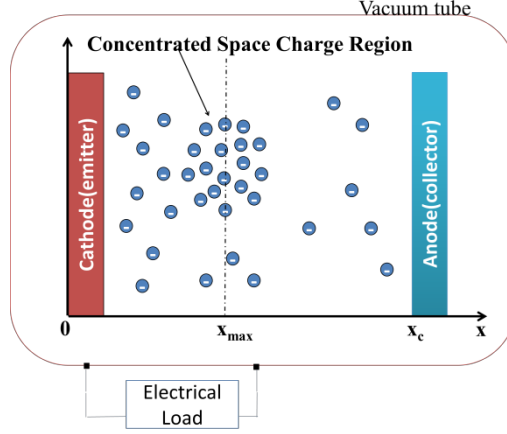


FIG. 2.1: Schematic diagram of SC formation in 1D-TECs. Note that electrons within the inter-electrode space form the SC and hinder the upcoming electrons to reach the collector.

In order to solve Eq. 2, we need to define the integration limits which can be expressed in terms of velocity of the electrons, i.e. for  $x \geq x_{max}$  the electrons have velocities in the range  $v_{x,min} < v(x) < \infty$  and for  $x < x_{max}$  in the range  $-v_{x,min}(x) < v(x) < -\infty$ , where  $v_{x,min} \equiv v_x(x_{max})$ . These limits state that the fraction of electrons which lack the energy to overcome the space-charge potential ( $x < x_{max}$ ) turn back towards the emitter while the electrons which surpass the space-charge potential ( $x > x_{max}$ ) can reach the cathode. After inserting these limits into Eq. 2, the space-charge density in the inter-electrode space is given by:

$$\rho(x) = 2q n_0 \left( \frac{m_e}{2\pi k_B T} \right)^{\frac{1}{2}} e^{-\frac{q \Phi_{SC}(x)}{k_B T}} \begin{cases} \int_{-\infty}^{-v_{x,min}} dv_x e^{-\frac{q \Phi_{SC}(x)}{k_B T} - \frac{v_x^2}{k_B T}}; x < x_{max} \\ \int_{v_{x,min}}^{\infty} dv_x e^{-\frac{q \Phi_{SC}(x)}{k_B T} - \frac{v_x^2}{k_B T}}; x \geq x_{max} \end{cases} \quad (3)$$

$$\text{Where, } v(x) \equiv \left[ \frac{2q}{m_e} (\Phi_{SC,max} - \Phi_{SC}(x)) \right]^{\frac{1}{2}}, \Phi_{SC,max} \equiv \Phi_{SC}(x_{max})$$

This equation can be reduced and simplified with the help of the Gaussian integral and error function [14]. By using Eq. 3 and the Poisson's equation (Eq.1), we finally obtain a self-consistent differential equation for the SC potential:

$$\Delta \Phi_{SC}(x) = -\frac{qn_0}{\epsilon_0} e^{-\frac{q}{k_B T} \Phi(x)} \left\{ 1 \pm \text{erf} \left[ \frac{q}{k_B T} (\Phi_{SC,max} - \Phi_{SC}(x)) \right]^{\frac{1}{2}} \right\} \quad (4)$$

The plus and minus signs indicate electrons accelerating under the condition that  $x < x_{max}$  and  $x \geq x_{max}$ , respectively. By considering the Richardson-Dushman current density  $J_{RD}$  which describes the initial current emitted from the cathode, the  $n_0$  quantity can be calculated as:

$$n_0 = \frac{J_{RD}(\phi_e, T)}{q} \left( \frac{\pi m_e}{2k_B T} \right)^{\frac{1}{2}} \quad (5)$$

$$\text{Where, } J_{RD}(\phi_e, T) = A_{RD} T^2 e^{-\phi_e/k_B T}; \quad A_{RD} = \frac{4\pi m_e k_B q}{h^3}$$

The parameters defining the operating conditions of 1D-TECs that we use to analyse and solve the SC potential (Eq. 4) and the initial charge density  $n_0$  include the Richardson-Dushman coefficient  $A_{RD}$ , cathode work function  $\phi_e$  (2.7 eV), the Boltzmann constant  $k_B$  and the Plank constant  $h$ . For solving Eq. 4 we have used the mathematical module of COMSOL Multiphysics (partial differential equation module) with the following boundary conditions of electrostatic potential:  $\Phi_{sc}(0) = 0; \Phi_{sc}(x_c) = 0$  ( $x_c$  representing the anode side):

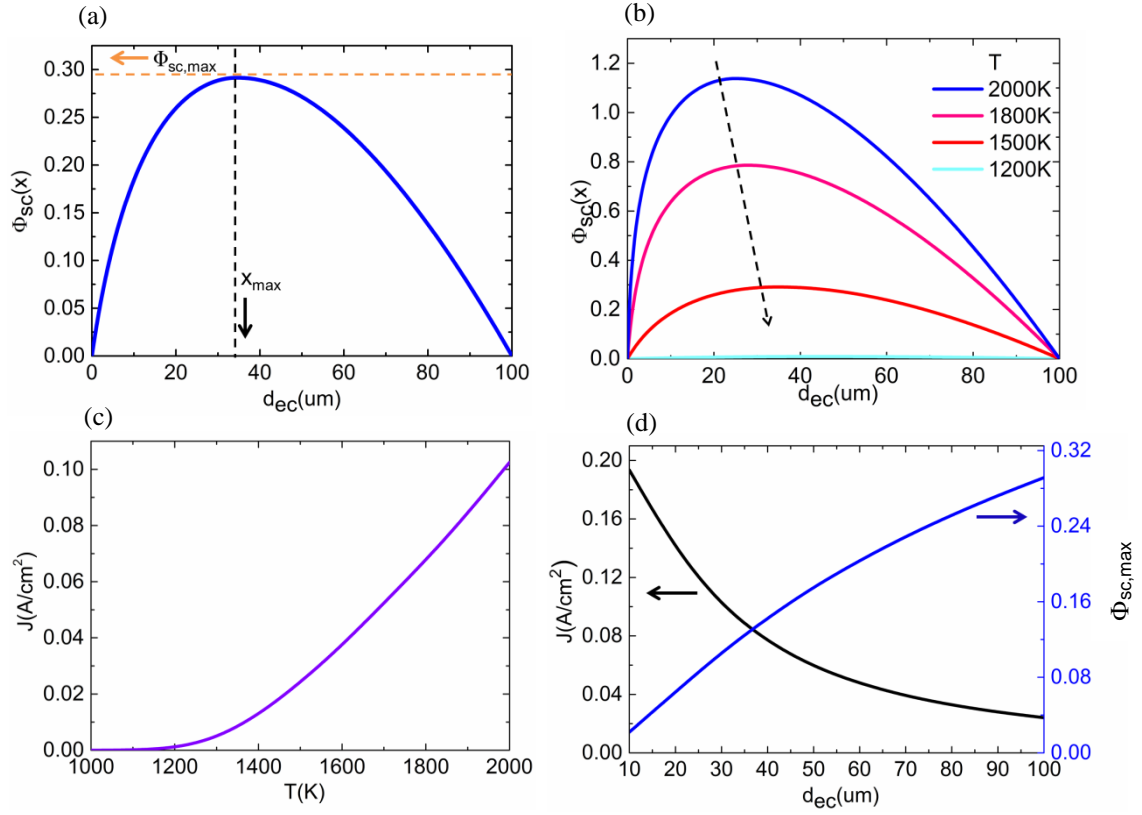


FIG. 2.2: (a) Space charge potential  $\Phi_{sc}(x)$  as a function of the inter-electrode space forms a maximum  $\Phi_{sc,max}$  at  $x=x_{max}$ . The electrons capable of overcoming  $\Phi_{sc,max}$ , can reach the cathode. The potential is calculated at  $T=1500$  K and  $d_{ec}=100$  μm. (b) Space charge potential as function of  $T$ . Note that by decreasing the temperature of the emitter (indicated by the arrow),  $\Phi_{sc}(x)$  decreases as well owing to the less amount of electrons excited at the emitter. (c) Net current density  $J$  as function of the emitter temperature  $T$  for  $d_{ec}=100$  μm. Note that by increasing the temperature of the cathode, the net current increases exponentially due to thermionic effect. (d) Net current density  $J$  (black curve) and space charge potential (blue curve) as function of the inter-electrode distance. Calculations are done at  $T=1500$  K with the Richardson-Dushman current density equal to  $0.22$  A/cm<sup>2</sup>.

The net current density  $J$  from 1D-TECs can be calculated from the following expression [14]:

$$J = J_{RD} e^{\frac{-q\Phi_{sc,max}}{k_B T}} \quad (6)$$

where  $J_{RD}$  is the saturation current, namely the current density at the emitter side. These calculations enable to predict the current density for 1D-TECs for different set-up parameters such as the emitter temperature and the inter-electrode distance  $d_{ec}$ .

As one can clearly see from Fig. 2.2(a), the space charge potential  $\Phi_{sc}(x)$  within the inter-electrode space forms a maximum  $\Phi_{sc,max}$  at the position  $x=x_{max}$ . Electrons which possess enough energy to overcome the maximum potential  $\Phi_{sc,max}$  can pass through and reach the anode (collector) so that they can be used to generate electrical power. Furthermore, the operating temperature of the emitter plays an important role in the performance of TECs, as it can clearly be seen from Fig. 2.2(b). By decreasing the temperature of the emitter,  $\Phi_{sc}(x)$  decreases as less electrons will be excited. In turn, this will affect the net current density  $J$  as shown in Fig. 2.2(c). One can clearly see that by increasing the temperature of the emitter the net current density increases as well. However this effect appears to have almost a neglectable on the net current density  $J$  in fact, even at values as high as  $T=2000$  K, the quantity  $J$  is  $0.102$  A/cm<sup>2</sup> upon a saturation current  $J_{RD}$  of  $75$  A/cm<sup>2</sup>. On the other hand, from the black curve of Fig. 2.2(d), it can be observed that the net current density  $J$  can be strongly increased by decreasing the inter-electrode distance  $d_{ec}$  as the space-charge potential decreases (blue curve). In Fig. 2.2(d) the considered temperature was  $1500$  K leading to a  $J_{RD}= 0.22$  A/cm<sup>2</sup>.

### 3. One Dimensional (1D) space charge Langmuir theory for Photon Enhanced Thermionic Emission

A PETE device comprises a p-type of semiconductor as emitter (cathode) and a metal plate collector (anode) with a vacuum gap in between them, as shown in Fig 3.1 [20]. Schwede et al. [20] theoretically estimated that PETE devices could surpass Shockley-Quiesser limit of an ideal single junction solar cell. Likewise in TECs, charge carriers form a space charge (SC) cloud within the inter-electrode vacuum space [26]. As mentioned, the formation of the space charge cloud significantly limits the practical applications in TECs [28,30]. In order to estimate this effect in a PETE device, we need to calculate the electrostatic space charge potential inside the inter-electrode gap which implies solving the self-consistent Poisson's equation, similarly to the procedure illustrated for the 1D case of TECs (see Eq. 4). The space charge theory explained here can be directly extended from the 1D model of G. N. Hatsopoulos et al. [29] theory on SC which was previously adopted by J. R. Smith et al. [31] and S. Shu et al. [23] to estimate the performance of TECs and PETE solar cells with the presence of space charge cloud.

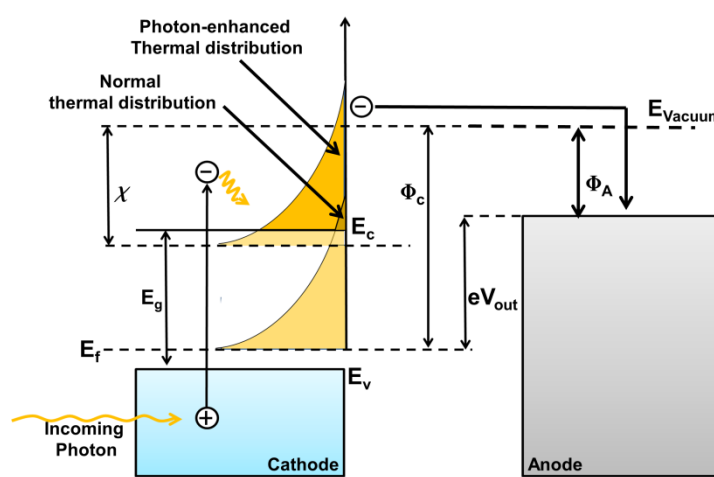


FIG. 3.1: Schematic energy diagram and working principle of photon-enhanced thermionic emission (PETE) solar cell. Electrons in the valence band are excited to the conduction band through the absorption of incoming photons and their thermalization. To leave the emitter surface, the electrons need enough energy to overcome the electron affinity  $\chi$ . If this current circuit is closed on a load ( $V_{out}$ ), the device could generate electricity. Note that through the photoelectric excitation the thermal energy contribution is modified and, with comparison to the normal thermal distribution, more electrons will be able to overcome the electron affinity.

The algorithm for space charge theory is divided into three sections based on the location of the carriers in the inter-electrode space and it can be described by means of the motive  $\psi(x)$  [23,29,31]. In particular,  $\psi(x)$  is

defined as the electrostatic potential times the negative elementary charge and it represents the barrier the electrons have to overcome to reach the anode. The three sections are defined as: i) Saturation regime (see Fig. 3.2(a)). The maximum value of  $\psi_m$  is found just outside the cathode surface. Thus without the presence of any extra barrier, electrons are free to move through the vacuum space to reach the anode (collector). ii) Space-charge regime (see Fig. 3.2(b)). In the presence of strong space charge cloud, the maximum motive lies inside the inter-electrode space thus the electrons have to overcome this barrier in order to reach the anode. iii) Critical regime (see Fig. 3.2(c)). The maximum motive value lies just outside the anode. The electrons have to overcome this decelerating force in order to reach anode. Under this condition the PETE cell works in a retarding mode [23].

The electrostatic potential, which is determined in terms of the motive  $\psi(x)$ , can be estimated by the Poisson's equation for a PETE solar cells [23]:

$$\Delta\psi(x) = -\frac{q\rho(x)}{\epsilon_0} \quad (7)$$

Where  $\rho(x)$  is the charge density between electrodes and  $\epsilon_0$  is the permittivity of free space. By defining  $\rho(x)$  in terms of  $\psi(x)$ , a self-consistent differential equation of the motive is obtained. The electron density can be calculated in terms of velocities of electrons within the different regions of the inter-electrode space:

$$\rho(x) = q \int_{-\infty}^{\infty} dv_x \int_{-\infty}^{\infty} dv_y \int_{-\infty}^{\infty} dv_z f(x, v_x) \quad (8)$$

where  $v_x$  is the velocity of electrons in x direction.

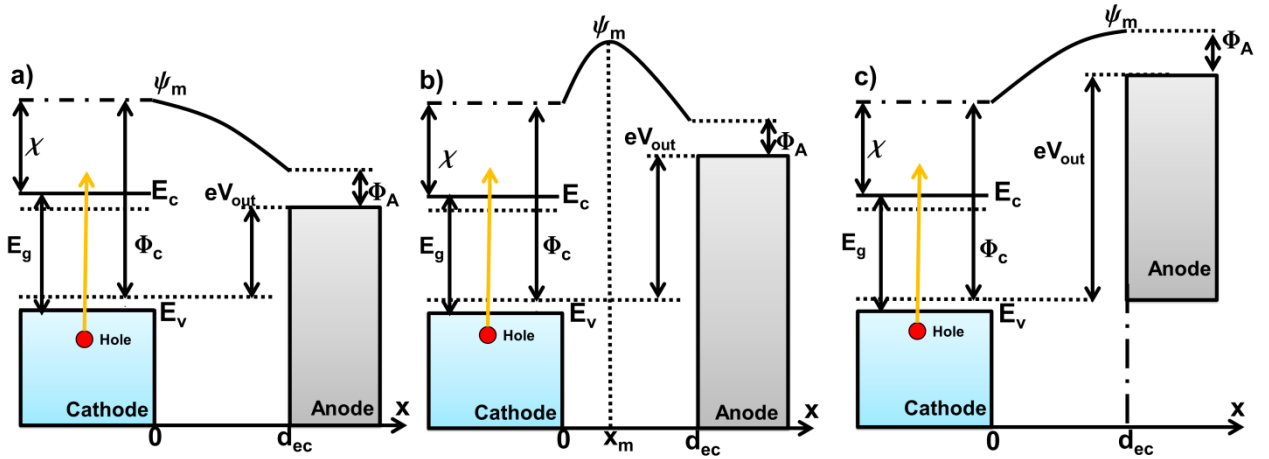


FIG. 3.2: Energy band diagram of SC theory for a PETE solar cell. (a) Motive diagram of the saturation regime where electrons can freely move to the anode side without any kind of obstruction from the negatively charged cloud. (b) Motive diagram of the space-charge regime where electrons have to overcome the maximum motive at  $x_m$ . (c) Critical regime, where electrons have to overcome the decelerating force.

Assuming now to have the PETE device working in the **Space-Charge Regime** (see Fig. 3.2(b)), the quantity  $f(x, v_x)$  can be written as follows:

$$f(x, v_x) = \frac{2\rho(x_m)}{q} \left( \frac{m_e}{2\pi k_B T_c} \right)^{\frac{3}{2}} e^{\frac{\psi_m - \psi(x)}{k_B T_c} - \frac{m_e v^2}{k_B T_c}} \begin{cases} \sigma(v_x - v_0), & x \geq x_m \\ \sigma(v_x + v_0), & x < x_m \end{cases} \quad (9)$$

Where  $v_0 = [-2((\psi_m - \psi(x))/m_e)]^{1/2}$  is the minimum velocity of electrons,  $T_c$  is the cathode temperature and  $\sigma$  represents the unit step function. By inserting Eq. 9 into Eq. 8, and with the help of the error function and the Gaussian integral [29], the electron density expression in space-charge regime can be written as [31]:

$$\rho_{SCR}(x) = \rho(x_m) e^{\frac{\psi_m - \psi(x)}{k_B T_c}} \begin{cases} 1 - \operatorname{erf}\left(\frac{\psi_m - \psi(x)}{k_B T_c}\right), & x \geq x_m \\ 1 + \operatorname{erf}\left(\frac{\psi_m - \psi(x)}{k_B T_c}\right), & x < x_m \end{cases} \quad (10)$$

By substituting Eq. 10 into Eq. 7, the following self-consistent motive distribution is obtained [23,29]:

$$2 \frac{d^2 \gamma}{d\xi^2} = e^\gamma \begin{cases} 1 - \operatorname{erf}(\gamma), & \xi \geq 0 \\ 1 + \operatorname{erf}(\gamma), & \xi < 0 \end{cases} \quad (11)$$

For convenient analysis, in Eq. 11 the quantities  $\gamma \equiv (\psi_m - \psi(x))/k_B T_c$  and  $\xi \equiv (x - x_m)/x_0$  are dimensionless, with  $x_0^2 = \partial_0 k_B T_c / 2q\rho(x_m)$  [31]. Now Eq. 11 can be solved to obtain the dimensionless motive profile within the inter-electrode space where the following boundary conditions are used,  $\gamma_{\xi=0} = 0$ ,  $(d\gamma/d\xi)_{\xi=0} = 0$ . After determining the dimensionless motive  $\gamma$  from Eq. 11, it can finally be substituted into  $\gamma = (\psi_m - \psi(x))/k_B T_c$ , to find the spatial distribution of  $\psi(x)$ .

The quantity  $f(x, v_x)$  can also be used to calculate the current density which depends on the number of electrons overcoming the maximum value of  $\psi_m$  and reaching the anode:

$$J_{SCR} = q \int_{-\infty}^{\infty} dv_x \int_{-\infty}^{\infty} dv_y \int_{-\infty}^{\infty} dv_z f(x_m, v_x) v_x \quad (12)$$

Once the dimensionless motive  $\gamma$  is solved through Eq. 11, the SC density can be determined by Eq. 9. Afterwards, by using the solution of Eq. 9 and substituting it into Eq. 12, the current density calculated at  $x = x_m$  (maximum potential) can be expressed as follows:

$$J_{SCR} = 2\rho(x_m) \left( \frac{k_B T_c}{2\pi m_e} \right)^{1/2} \quad (13)$$

Similarly, the current density  $J_{SR}$  calculated in **Saturation Regime** (Fig. 3.2(a)) can be written as:

$$J_{SR} = q \int_{-\infty}^{\infty} dv_x \int_{-\infty}^{\infty} dv_y \int_{-\infty}^{\infty} dv_z f(0, v_x) v_x \quad (14)$$

and the relationship between the net current density  $J$  and saturation current density can be expressed as:

$$J = J_{SR} e^{-\gamma_c} \Rightarrow \gamma_c = \ln \frac{J_{SR}}{J} \quad (15)$$

where  $\gamma_c \equiv \gamma(x=0)$ . More specifically, the saturation current density can be calculated by the following expression at a given energy band gap  $E_g$ , temperature  $T_c$  and electron affinity  $\chi$  [20,23]:

$$J_{SR} = qn_0 \sqrt{\frac{k_B T_c}{2\pi m_e}} e^{-\chi/k_B T_c} \quad (16)$$

Similarly, the voltage in saturation regime  $V_{SR}$  can also be estimated with the following conditions i.e.  $\xi_C \equiv \xi(x=0) = 0$  and  $\xi_A \equiv \xi(x=d_{ec}) = (2J m_e q^2 / \partial^2_0 k_B^3)^{1/4} J_s^{1/4} d_{ec} / (T_c)^{3/4}$  in Eq. 11. The result is [23]:

$$V_{SR} = (\phi_c - \phi_A - \gamma(\xi_A) k_B T_c) / q \quad (17)$$

Where  $\phi_c$  and  $\phi_A$  are respectively the work functions of cathode and anode and  $\gamma(\xi_A)$  is the dimensionless motive at the anode side which can be calculated from Eq. 11.

Moving now to analyze the **Critical Regime** (Fig. 3.2(c)), the critical current density and voltage can be calculated as:

$$J_{CR} = qn_0 \sqrt{\frac{k_B T_c}{2\pi m_e}} e^{-\frac{\chi + (\phi_A + qV - \phi_c)}{k_B T_c}} \quad (18)$$

and

$$V_{CR} = [\phi_c - \phi_A - \ln(J / J_{CR}) k_B T_c] / q \quad (19)$$

Now, to provide an idea of the actual procedure we have followed to numerically calculate both the density current and the voltage, we show the steps taken for the case of space-charge regime:

- i. Choose a current density  $J_{SCR}$  such that  $J_{CR} < J_{SCR} < J_{SR}$ .
- ii. Calculate the barrier height for the emitted electrons from the cathode surface,  $\gamma_c$  from Eq. 15.
- iii. Calculate the corresponding dimensionless distance of the maximum motive from the cathode  $\xi(\gamma_c)$ , from Eq. 11.
- iv. Calculate the dimensionless distance between the maximum motive and the anode,  $\xi = (d_{ec}/x_0) - \xi(\gamma_c)$ .
- v. Finally, calculate the value of the motive of the barrier height from the anode  $\gamma_{Am}$  which can be given by Eq. 11. The voltage in space-charge regime can be expressed as follows [23,32]:

$$V_{SCR} = [(\phi_c + \gamma_c k_B T_c - \phi_c) - (\phi_A + \gamma_a k_B T_c)] / q \quad (20)$$

Once the current-voltage relations are estimated for all the three regimes, the related power output density  $P_{out}$  and power conversion efficiency  $\eta$  of PETE device can be expressed as follows:

$$P_{out} = \begin{cases} qn_0 V \sqrt{\frac{k_B T_c}{2\pi m_e}} e^{-\chi/k_B T_c}; 0 < V < V_s \\ J[(\phi_c + \gamma_c k_B T_c - \phi_c) - (\phi_A + \gamma_a k_B T_c)] / q; V_s < V < V_c \\ qn_0 V \sqrt{\frac{k_B T_c}{2\pi m_e}} e^{-\frac{\chi + (\phi_A + qV - \phi_c)}{k_B T_c}}; V_c < V \end{cases} \quad (21)$$

$$\eta = \frac{P_{out}}{P_{sun}} \quad (22)$$

Where,  $P_{sun}$  is the concentrated AM0 zero air mass solar spectral irradiance. The following is the list of parameters used in the computation:

Parameter	Value
Energy Gap ( $E_g$ )	1.5 eV
Electron affinity ( $\chi$ )	0.9 eV
Cathode Temperature ( $T_c$ )	1000 K

Table 1: Parameters of photon enhanced thermionic emission solar cells [23].

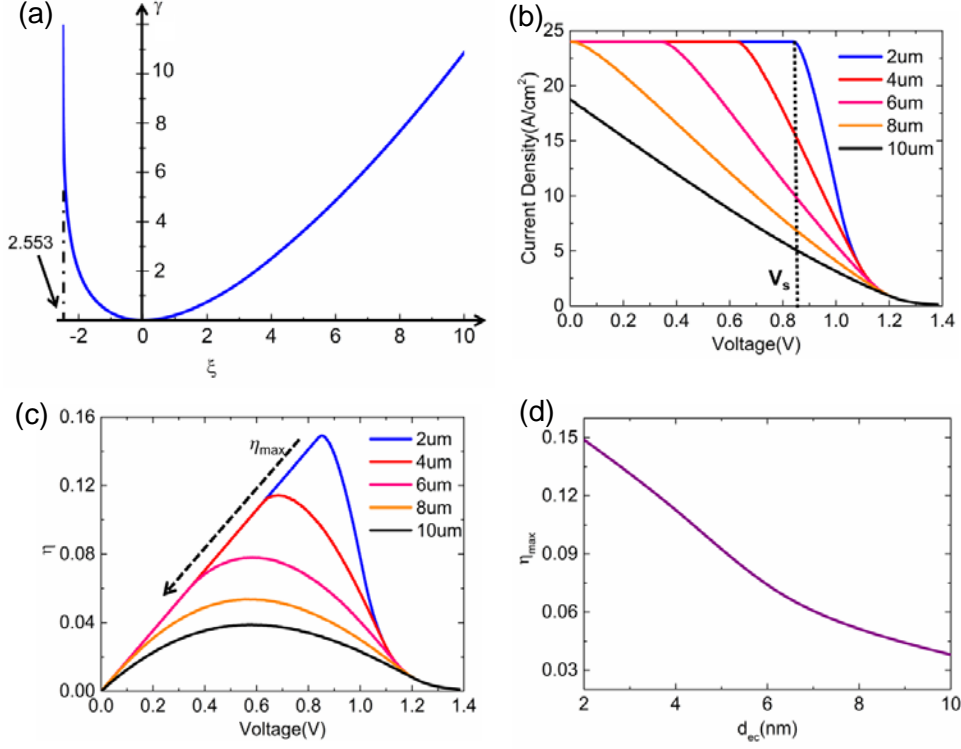


FIG. 3.3: (a) Dimensionless motive  $\gamma$  as a function of the dimensionless quantity  $\xi$  for a PETE solar cell. (b) The current-voltage relationship of PETE solar cell. Notice that by increasing the inter-electrode space ( $d_{ec}$ ), the space-charge cloud becomes dominant and the maximum current drawing from the device start decreasing. (c) Power conversion efficiency  $\eta$  as a function of the operating voltage  $V$  of PETE solar cell. Likewise, in the case of increasing the inter-electrode gap the efficiency of the device decreasing (indicated by the arrow). (d) Maximum efficiency  $\eta_{max}$  as a function of the distance between cathode and anode.

In Fig. 3.3(a) it is shown the relation between the dimensionless quantities  $\gamma$  and  $\xi$ . Furthermore, in Fig. 3.3(b) is illustrated the effect of the distance between the electrodes on the current density. In particular, the smaller  $d_{ec}$  the higher the current density. In voltage range  $0 < V < V_s$ , the device works in saturation regime, as all the emitted electrons overcome the barrier and will reach the anode (flat band condition). The electric current in this region is calculated by Eq. 16. In the space-charge regime, the maximum motive lies in the inter-electrode space. Near saturation point  $V_s$ , the maximum motive starts increasing while increasing the voltage and the electrons have to overcome this barrier in order to reach at anode and the net current density from the device is calculated by the number of electrons which can overcome the maximum motive. From Fig. 3.3(b), one can clearly see that the current density starts decreasing as less amount of electrons reach the anode. When no electrons can overcome the maximum motive, and the net current drawn from the device becomes zero, the critical regime is reached. While increasing the inter-electrode gap  $d_{ec}$ , the J-V curves shift to the left indicating a more pronounced influence of the charge cloud. In Fig. 3.3(c) the power conversion efficiency  $\eta$  is illustrated. Similarly to the current density, while increasing the voltage, the efficiency of the device increases but when electrons face the barrier (maximum motive) the efficiency starts decreasing. Moreover, Fig. 3.3(d) shows the monotonous decrease in the maximum efficiency as function of the inter-electrode gap obtained from the

device which shows that one can reduce the effect of the charge cloud by decreasing the distance between cathode and anode.

We have presented the effect of charge cloud in a photon enhanced thermionic emission device by employing an updated version of the one dimensional Langmuir theory. In this model, we have used finite element solver to reproduce the results for 1-D space charge problem reported by S. Shu et al. [23]. The main result was to find that the charge cloud effect can be noticeably reduced by decreasing the gap between electrodes. In the next section we shall approach the description of realistic devices by introducing a 3D-PETE model. In this regard, we have investigated the possibility of reducing the detrimental effect of charge cloud i) by employing a gate structure within the inter-electrode gap, ii) by considering the use of nanostructures on the cathode face.

#### **4. 3D space charge model for Photon Enhanced Thermionic Emission solar cells**

In the previous section we have introduced our 1D photon enhanced thermionic emission solar cell model for estimating the charge cloud effect. In particular, we have calculated the charge density within the inter-electrode space and estimated its influence on the efficiency of the device. The limitation of the illustrated model lies in the unrealistic 1D assumption similarly to the Langmuir theory [24]. Here we shall redefine the charge cloud computational model to 3D for an effective description of a realistic device.

The 3D finite elements based model is based on electron emission model by taking into account the three dimensional Maxwell-Boltzmann distribution of velocities and a random initial velocity direction and emission point on the cathode surface. Emission velocities are characterized by a polar and azimuthal angles  $\theta$  and  $\phi$ . The current density is then computed through an iterative process solved by means of COMSOL Multiphysics®. The model performs a bi-directional coupling between the particle tracing module and electrostatic modules of COMSOL. The net current density is determined from the electrons trajectories and the electric potential, calculated in a self-consistent way. Furthermore, in our model we have also introduced a successive-over-relaxation [33] feature to solve the problem of convergence in presence of high emitting current densities from the cathode surface, which we will explain in the next section. From the calculation we extract the desired information about electron emission, charge cloud formation and electron trajectories. The amount of net current produced by the device can be estimated. Consequently, we are also able to determine the power conversion efficiency.

Within the 3D finite elements based model, we have proposed a method for mitigating the space charge cloud problem. By inserting a positively charged gate electrode, towards which electrons are accelerated from the cathode, the space charge cloud effect is in fact reduced. We have estimated the role of the gate over the efficiency of the device by including the external power needed to sustain the gate electrode potential. Finally, we also made an attempt to improve the device performance by considering a nanostructured cathode surface in the form of an array of closely spaced nanocones. In the presence of an applied anode voltage a high electric field is expected at the cone apex, due to the tip effect. This is expected to increase the saturation current, since a locally enhanced electric field allows to reduce the local potential barrier for the electrons inside the semiconductor and hence to locally increase the extracted current. The effect is taken into account in the simulations in a self-consistent way. In addition, a saturation current enhancement is also expected due to the increased cathode surface area.

##### **4.1. Working principle, structural and simulation model details**

Our proposed architecture consists of a p-type GaAs cathode separated by a vacuum gap from a metal anode as shown in Fig. 4.1. As explained in our work [34], we chose GaAs as a cathode as it is the reference material

for photovoltaic technology to the extent that it has been recently used also for the experimental realization of PETE devices [20,35]. Importantly, the present model can however be adapted for investigating different kinds of materials such as GaN, known to exhibit better high temperature stability.

For what concerns the proposed simulation model, we have used a two-way-coupling iterative process implemented by means of COMSOL Multiphysics, in which particle trajectories and electrostatic potential are computed self-consistently in alternating steps to estimate the influence of space-charge effects. Particle trajectories and the electric potential are computed through time-dependent and stationary solver, respectively. The solver sequence goes through these two solvers for a specified number of iterations, always using the previous solution as input for the next iteration. In this way, a self-consistent solution, in which the particle trajectories and the electric potential affect one another, is obtained. We notice that this approach avoids considering explicitly the columbic electron-electron repulsion, which is much more computational demanding. The algorithm can be described by the following points:

- i. A fixed number of sample electrons is emitted at cathode surface with uniform random emission points and uniform random hemispherical angular distribution, while electron velocities are sampled from a half-Maxwellian distribution.
- ii. Each trajectory is computed by solving the equations of motion within the domain. No inter-electron force is assumed. The solution time is set to be long enough to allow for all the electrons to reach one of the boundaries of the computational domain. Each particle is assumed to release a spatial charge proportional to the transit time across each mesh element.
- iii. The electrostatic solver solves the Poisson's equation in presence of the space charge cloud computed at step (ii). The electrostatic potential is obtained.
- iv. The tracing process (see step ii) is then repeated, based on the updated potentials, until a self-consistent solution to the steady state current flow is found or the maximum iteration number is reached.

One known problem of the outlined iterative procedure i-iv is the poor convergence, or non-convergence at all, in case of high saturation currents (high electron emission rates). Actually, the potential distribution at the beginning of the computation process defines a situation with no charges inside the problem space. If the charge calculated from such a potential distribution is emitted, it would result in a sudden fluctuation in the potential distribution inside the problem space which is unphysical. This change in the potential distribution would then effect the charge that is to be emitted in the following iteration cycles. The cumulative error would finally result in an oscillatory solution that would not converge towards the actual solution.

As already mentioned, the convergence error can be cured by adopting a successive over relaxation algorithm [33,36], by which the charge cloud assumed at each iteration is given by:

$$\rho_n = \rho_n \omega + (1 - \omega) \rho_{n-1} \quad (23)$$

where  $\rho_n$  and  $\rho_{n-1}$  are the charge potentials calculated at  $n^{th}$  and  $(n - 1)^{th}$  time steps. The convergence solution of the numerical model will depend on the initial guess of the relaxation factor  $\omega$  and has to be adjusted according to the rate of convergence [36]. If the charge potential in a time step exceeds that of the previous time step, it is evident that the solution is diverging and the iterative process is terminated. A new relaxation factor is then selected [36]. By doing so, successive better approximations of the current can be computed. A. Knox et al. [33] used a similar kind of algorithm to demonstrate 3D electron emission model for thermionic devices.

Simulations were performed for a finite portion of the cathode emitting surface applying elastic "bounce" boundary conditions at the domain sides, hence mimicking periodic boundary conditions, as shown in Fig. 4.1(a). The anode-cathode distance and the period of the cell are denoted by  $d_{ec}$  and  $P$ , respectively, as shown

in Fig. 4.1(b). In particular, the figures show the directions of electrons from the cathode with respect to the polar angle  $\theta$  and an azimuthal angle  $\phi$ . If  $\tau$  is a random variable in the range  $0 < \tau < 1$ , then the azimuthal angle is given by [37]:

$$\phi = 2\pi\tau \quad (24)$$

Assignment of the polar angle was weighted so that there were equal numbers of electrons per solid angle in the emission hemisphere:

$$\theta = \sin^{-1}(\tau) \quad (25)$$

The initial direction-vector components of velocity of emission electrons with respect to emission angles( $\theta, \phi$ ) can be expressed as [37] follows:

$$\begin{aligned} v_x &= v \cos(\theta) \cos(\phi) \\ v_y &= v \cos(\theta) \sin(\phi) \\ v_z &= v \sin(\theta) \end{aligned} \quad (26)$$

To assign the kinetic energy of emission electrons from cathode, the Maxwell-Boltzmann distribution is used with the respect to the cathode temperature  $T_c$ , thus the probability distribution which includes all the directions (x,y,z) can be expressed [33]:

$$f(\mathbf{v}) = 4\pi \left( \frac{m_e}{2\pi k_B T} \right)^{\frac{3}{2}} v^2 e^{-\frac{m_e v^2}{2k_B T}} \quad (27)$$

Where  $m_e$  is the mass of the electron and  $\mathbf{v} = \sqrt{v_x^2 + v_y^2 + v_z^2}$  is the electron velocity.

As mentioned (Eq. 22), the power conversion efficiency is defined as  $\eta = P_{out}/P_{in}$  where  $P_{in}$  can be calculated from AM0 solar irradiance [39].  $P_{out}$  is instead the power density delivered to the load, which is given by [38]:

$$P_{out} = \left( \frac{\phi_c - \phi_a}{q} - V \right) J \quad (28)$$

Here  $\phi_c$  and  $\phi_a$  are the work functions of cathode and anode, respectively,  $J$  is the net current density and  $V$  is the load voltage. The work function of the cathode is  $\phi_c = E_c - E_f + \chi_c$ , being  $E_f$  the Fermi-level of GaAs which can be expressed as  $E_f = 0.034 + 1.5 \times 10^{-14}(T_c - 273) + 7.6 \times 10^{-14}(T_c - 273)^2$  [15] and  $E_c$  the conduction band edge given by  $E_c = E_g - E_f$  with  $E_g$  the band gap of GaAs. The net current density  $J$  is determined by calculating the ratio between the number of electrons reaching the anode  $N_a$  to the number of electrons emitted from the cathode  $N_c$ :

$$J = \frac{N_a}{N_c} J_s \quad (29)$$

Where  $J_s$  is the saturation current density which is calculated from Eq. 16.

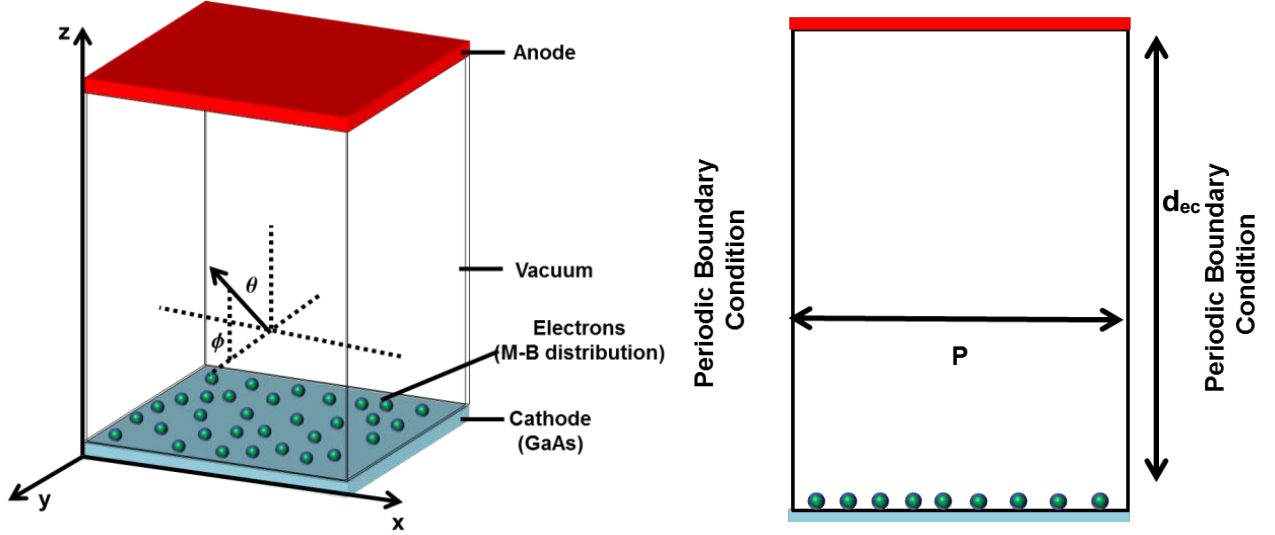


FIG. 4.1: (a) Schematic diagram of photon enhanced thermionic emission solar cell where electrons are randomly distributed in the ‘x-y’ plane and excited randomly in ‘z’ direction with polar angle  $\theta$  and in-plane angle  $\phi$ . The velocities of the electrons are organised according to the Maxwell-Boltzmann distribution. Notice that electrons are excited through the semiconductor (GaAs) in the vacuum where they form a negatively charge cloud. Electrons which can overcome the cloud can reach the anode and participate in the electricity generation. (b) 2-D cross-section (x-z) of the architecture, where periodic boundary conditions are imposed on the side boundaries.

## 4.2. Results and Discussion

In the following discussion we shall consider the AM0 solar irradiance as the incident spectrum. The cathode is p-type GaAs semiconductor with acceptors concentration equal to  $10^{19}\text{cm}^{-3}$  and band-gap of 1.5eV. In Table 2 the list of parameters considered in our simulation model.

Parameter	Value
Energy Gap ( $E_g$ )	1.5 eV
Electron affinity ( $\chi$ )	0.4 eV
Cathode Temperature ( $T_c$ )	1000 K
Saturation Current Density ( $J_s$ )	20 A/cm <sup>2</sup>
Anode work function ( $\phi_a$ )	0.9 eV
Number of particles at Cathode ( $N_c$ )	1000
Period (P)	1 $\mu\text{m}$
Inter-electrode distance ( $d_{ec}$ )	20 $\mu\text{m}$

Table 2: Parameters of photon enhanced thermionic emission solar cells.

Fig. 4.2(a) describes the space charge potential  $\Phi_{sc}(z)$  calculated within the inter-electrode gap. At  $z=z_{\text{max}}$  it forms a maximum  $\Phi_{sc,\text{max}}$  which electrons need to overcome in order to reach the anode. Similarly, the maximum current density  $J_{\text{max}}$  is plot in Fig. 4.2(b) (blue curve). It can be observed that  $J_{\text{max}}$  can be strongly increased by decreasing the inter-electrode distance  $d_{ec}$  as the space-charge potential decreases (red curve). Fig. 4.2(c) shows the current-voltage curves while increasing the inter-electrode distance  $d_{ec}$  from to 2  $\mu\text{m}$  to 20  $\mu\text{m}$ . The period is equal to 1  $\mu\text{m}$ . In particular, for  $d_{ec}=2 \mu\text{m}$  both the results from 1D and 3D are shown. The plots suggest a qualitative agreement between the two models. In fact, the figure clearly shows that for 2 $\mu\text{m}$  inter-electrode distance all electrons overcome the barrier (space charge potential) and reach the anode up to a point when space-charge potential becomes dominating, and less amount of electrons can pass through the barrier so that the net current starts decreasing. Furthermore, when the space-charge potential becomes so prominent that no electrons can overcome the barrier, the net current becomes zero. In addition, we have also calculated the efficiency  $\eta$  of the device as shown in Fig. 4.2(d). The maximum efficiency calculated for 2  $\mu\text{m}$

is 7.8% which reduces upon increase of  $d_{ec}$  down to 1% for 10  $\mu\text{m}$  gap. From the 3D numerical model, one can trace down the trajectories of electrons travelling from the cathode to the anode in order to investigate the influence of the charge cloud on the net current extracted from the device.

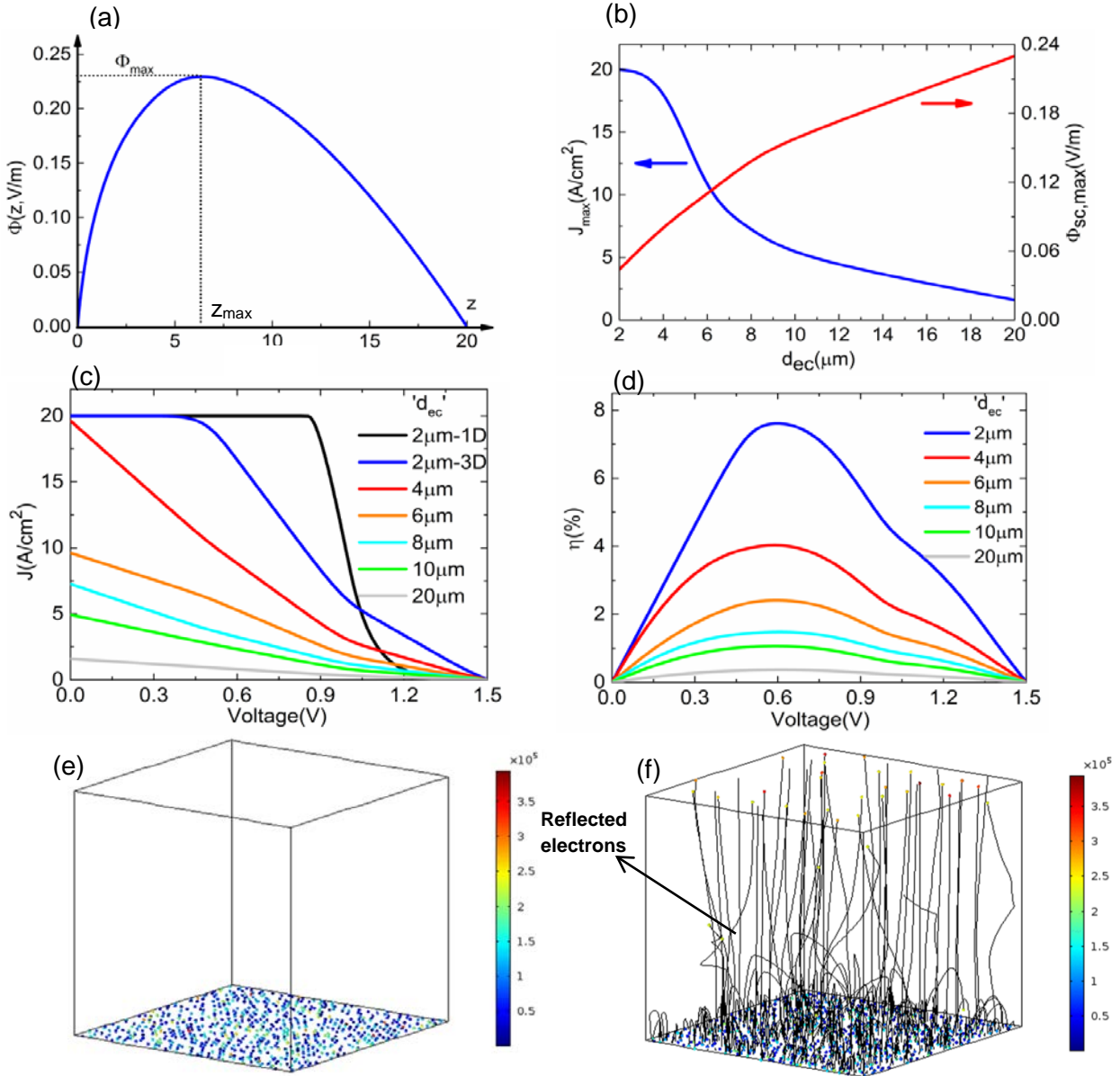


FIG. 4.2: (a) SC potential  $\Phi(z)$  when cathode and anode are at the same electrostatic potential  $V=0$ . Note that the electrons have to overcome  $\Phi(z)$  in order to reach the anode to generate electricity. (b) Maximum current density  $J_{max}$  (blue curve) as function of inter-electrode distance. It decreases by increasing the distance due to the enhancement of the space charge potential ( $\Phi_{sc,max}$  red curve, right). The calculation is done at  $T=1000$  K and with saturation current density equal to  $20 \text{ A}/\text{cm}^2$ . (c) Current-voltage relationship of PETE solar cell. Notice that by increasing the inter-electrode space ( $d_{ec}$ ), the space charge cloud becomes dominant and the maximum current drawing from the device start decreasing. (d) Power conversion efficiency ( $\eta$ ) as function of the operating voltage (V) of PETE solar cell. Upon increase of the inter-electrode space, the efficiency of the device decreases. (e) At  $t=0$  electrons are at the cathode with a random spatial distribution. The colours represent the velocity in m/s. Their distribution follows the Maxwell-Boltzmann statistics. Box base:  $1 \mu\text{m} \times 1 \mu\text{m}$ , box height  $10 \mu\text{m}$ . (f) Trajectories of the emitted electrons. The influence of the charge cloud determines back reflection towards the cathode of some of the electrons. Distance between cathode and anode is  $10 \mu\text{m}$  with a saturation current density of  $20 \text{ A}/\text{cm}^2$ . Box base:  $1 \mu\text{m} \times 1 \mu\text{m}$ . Scale bar: velocity in m/s.

From Fig. 4.2(e) we can observe that at time  $t=0$  all the electrons are at the cathode surface. At a later stage, after leaving the cathode, some of them return back due to charge cloud effect while others have enough energy to overcome the barrier thus to reach the anode, as shown in Fig. 4.2(f). In the present plots the distance

between the cathode and the anode is 10  $\mu\text{m}$ . From these results we could conclude that above certain  $d_{ec}$  gaps, the charge cloud effect can be remarkably severe on the power conversion efficiency  $\eta$  to limit the actual application of a PETE device. In this regard, in the next section we are going to investigate a different approach to improve the efficiency  $\eta$  besides  $d_{ec}$  reduction.

## 5. 3D gate insertion for resolving the space-charge problem for PETE device

As we explained at earlier stage, photon enhanced thermionic emission utilizes the photoelectric and thermal effects to enhance electrons emission. Theoretically, it was shown that PETE can beat the Shockly-Quiesser limit of single junction photovoltaics cells [17], however turning this elegant theoretical device into a commercially available one is a challenging task especially due to the charge cloud effect and thermal instabilities. In the previous section we have shown that the net current density  $J$  from the device is significantly suppressed for inter-electrode distances greater than 2  $\mu\text{m}$ . In this regard, a method to limit the negative effect of charge cloud was recently suggested [25]. The idea was to insert  $\text{Cs}^+$  ions into the vacuum chamber (inter-electrode gap). A different method was introduced by S. Meir et al. [15] where they used a positively charge gate electrode located inside the inter-electrode gap. The gate electrode accelerates the electrons away from the cathode and decelerates them as they approach the anode. In this way the charge cloud effect is reduced and the power conversion efficiency is increased. Along with these findings, we have introduced a gate in our 3D numerical model.

### 5.1. Simulation model details, results and discussion

We have inserted a positively charged gate terminal in the middle of the inter-electrode gap, constituted by a squared thin wire mesh. Fig. 5.1(a) shows the schematic diagram of the proposed architecture. As simulation setup, we took the same simulation model already implemented for the 3D PETE solar cell. Simulations were performed for an infinitely extended square array by applying periodic boundary conditions with period  $P$  along  $x$  and  $y$  directions, as defined in Fig. 5.1(b). The width of the gate terminal is denoted by  $G$  as shown in Fig. 5.1(b). The overall device efficiency can be expressed as follows:

$$\eta = \frac{P_{out} - P_g}{P_{in}} \quad (30)$$

Where,  $P_{out}$  is the power density delivered to the load calculated through Eq. 28,  $P_{in}$  is the incident power density calculated from AM0 spectrum irradiance and  $P_g$  is the power density required to feed the gate. Electrons reaching the gate cause a current density  $J_g$ . To maintain the gate voltage, a power density of  $P_g = J_g V_g$  has to be provided, which leads to an additional energy loss in the PETE device. The  $J_g$  can be calculated by calculating the ratio of number of electrons reaching the gate to the number of electrons emitted from the cathode ( $N_g/N_c$ ) can be expressed as follows:

$$J_g = \frac{N_g}{N_c} J_s \quad (31)$$

Where  $J_s$  is the saturation current density which is calculated from Eq. 16. In the present simulation model, the same list of parameters mentioned in Table 2 has been employed.

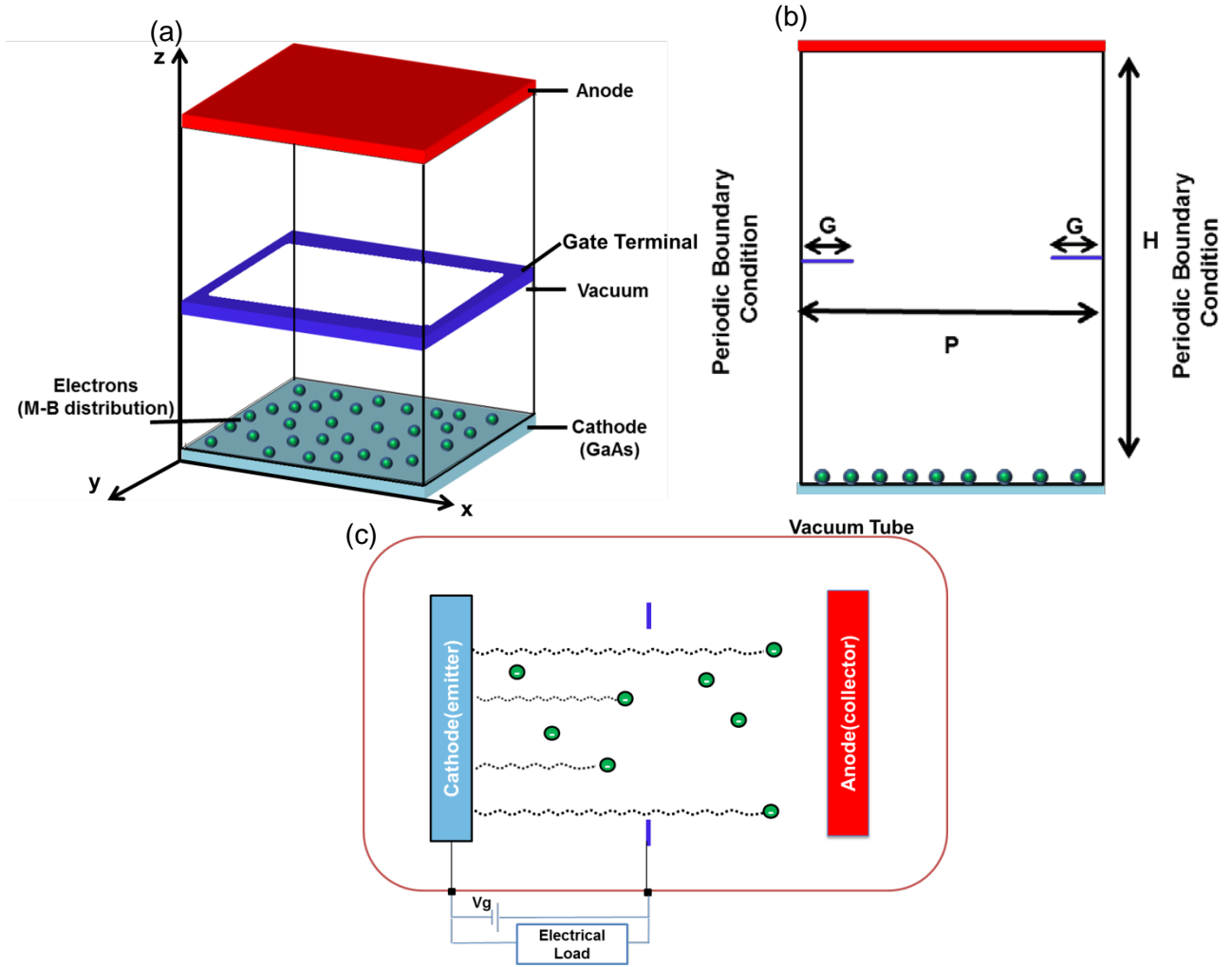


FIG. 5.1: (a) Proposed schematic diagram of a photon enhanced thermionic emission solar cell with a positively charged gate inserted in the vacuum chamber. (b) 2-D cross-section ( $x$ - $z$ ) of the proposed architecture, where periodic boundary conditions are employed on side boundaries. (c) Schematic circuit diagram of the proposed architecture.

In the present calculations the inter-electrode distance is  $20\ \mu\text{m}$  and the width of the wires constituting the gate terminal is  $P/10$ . We point out that the wires should be thin enough to guarantee a sufficient amount of electrons channelling through the hole thus to reach the anode. Later on, a detailed optimization with respect to the gate size and period will be evaluated to maximize the performance of the device. Initially, in order to understand the role of gate terminal, both cathode and anode are taken at the same electrostatic potential  $V=0$ .

Fig. 5.2(a) shows the calculated electrostatic potential  $\Phi(z)$  in the inter-electrode space. In case of gate-free condition, there is strong electrostatic potential within the inter-electrode space (blue curve). Upon switching on the gate voltage  $V_g$ , the space-charge potential is reduced. However, a minimum value of the gate voltage is required to completely suppress the space-charge potential (see Fig. 5.2(b)). For example, when  $V_g=1\ \text{V}$ , a potential near the cathode is still present (Fig. 5.2(a), red curve). For higher values of gate voltage, the space-charge potential diminishes as shown in Fig. 5.2(b). Furthermore, from our 3D numerical model, one can trace down the trajectories of the electrons travelling from the cathode to the anode in order to highlight the influence of the positively charged gate on the charge cloud. Fig. 5.2(c) shows the velocity and position distribution of electrons at  $V_g=0\ \text{V}$ . Clearly, in the absence of gate terminal, most of the electrons are at the cathode surface, in fact only the electrons which can overcome the potential barrier can indeed reach the anode. In particular, starting from  $N_c=1000$ , it was obtained  $N_a=39$ . On the other hand, when the gate terminal is inserted with a positive gate voltage  $V_g=2\ \text{V}$ , 448 electrons reach the anode surface as shown in Fig. 5.2(d). Even though inserting a gate can have positive effects on reducing the charge potential, it happens that some electrons are absorbed by the gate itself thus generating a gate current estimated through Eq. 31. As we are giving an

additional power density in the form of gate terminal, the gate power density needs to be taken into account in order to estimate the net efficiency from the PETE device as shown in Eq. 30.

In Fig. 5.3(a) is shown the J-V characteristics upon  $V_g$  change. It is found that the higher  $V_g$  the higher is the net current density, namely the power extracted from the device. In Fig. 5.3(b) is illustrated the net efficiency  $\eta$  versus the applied voltage as calculated from Eq. 30. To calculate the net efficiency, we have considered also the amount of external energy consumed by the gate. This effect is calculated through Eq. 30 and 31. Similarly to Fig. 5.3(a), the power conversion efficiency  $\eta$  increases by increasing the gate terminal voltage.

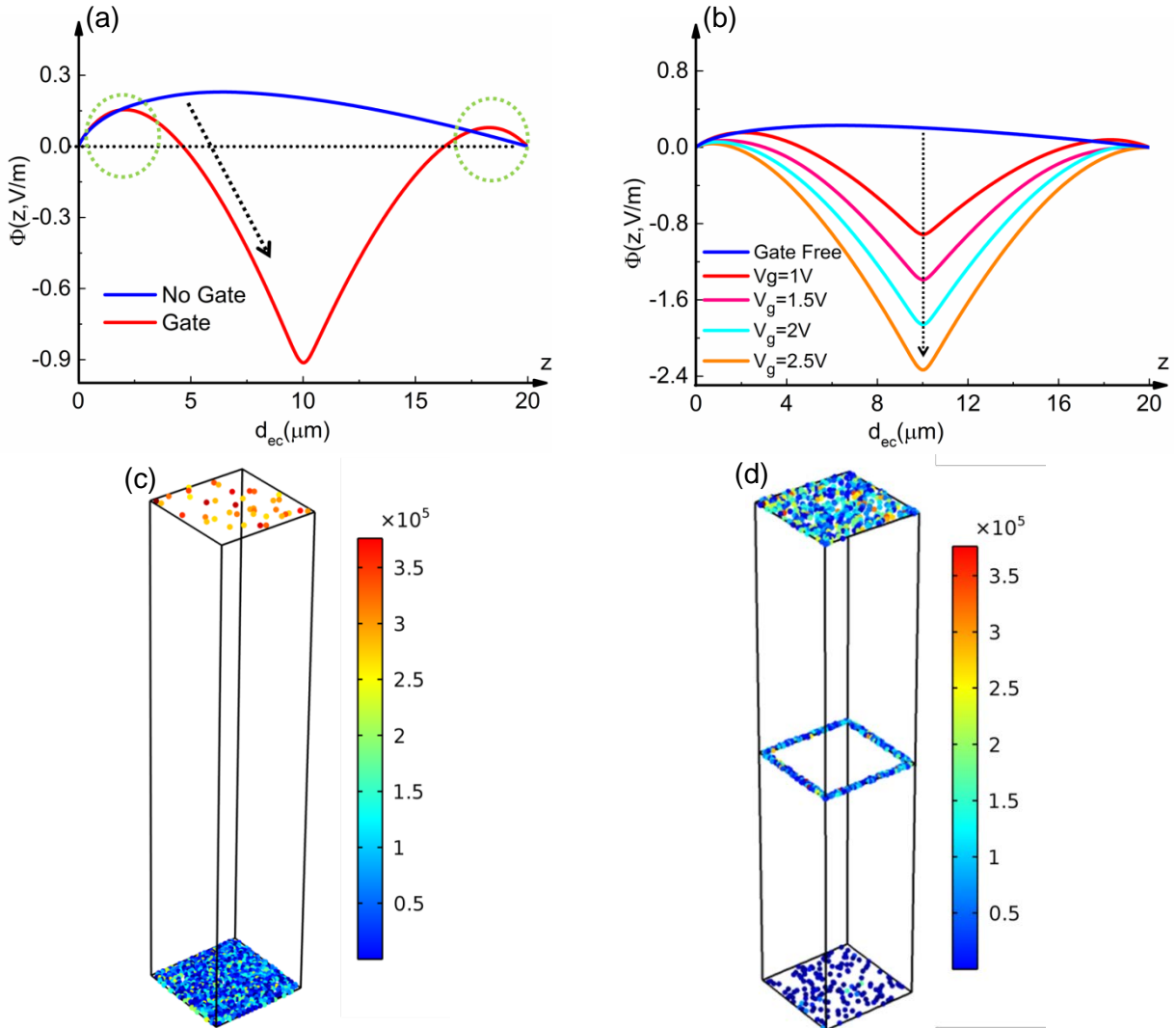


FIG. 5.2: (a) Calculated space charge potential  $\Phi(z)$  under no gate condition (blue curve) and with gate voltage  $V_g=0.5$  V (red curve). Upon switching on the gate voltage, the space charge potential is reduced (black arrow). (b) Calculated space charge potential for gate voltages between 0 V and 2 V. The higher  $V_g$ , the lower  $\Phi(z)$ . (c) Random distribution of electrons with respect to their velocity and position at  $V_g=0$  V. Note that at  $t=14$  ns, most of the electrons are at the cathode and only those which can overcome the strong potential can reach the anode. (d) Random distribution of electrons with respect to their velocity and position with  $V_g=2$  V. With respect to (c), a higher number of electrons can reach the anode, namely an enhancement of the net current is observed (see Eq. 31). In all calculations  $d_{ec}=20$   $\mu\text{m}$ .

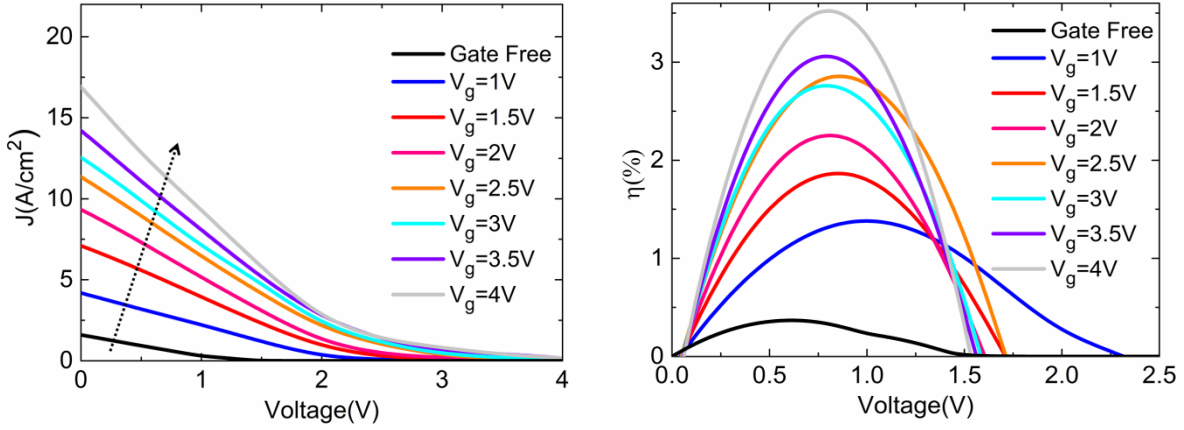


FIG. 5.3: (a) Current-Voltage characteristics of a PETE device by changing the gate terminal voltage  $V_g$ . Note that, while increasing the gate voltage, the net current of the device increases as well (black arrow). (b) Power conversion efficiency  $\eta$  versus operating voltage  $V$  upon change of the gate terminal voltage  $V_g$ . The power conversion efficiency  $\eta$  increases while increasing the gate voltage which is due to the enhancement of the net current  $J$ . In all calculations  $d_{ec}=20\ \mu\text{m}$ .

## 5.2. Gate Insertion: Parametric optimum design

In the above explanation, we have investigated and proved the advantageous role of a gate terminal in reducing the charge cloud effect and enhancing the power conversion efficiency of a PETE device. Here, we are going to generalize these results by optimizing the pitch size and by demonstrating its influence on the power conversion efficiency.

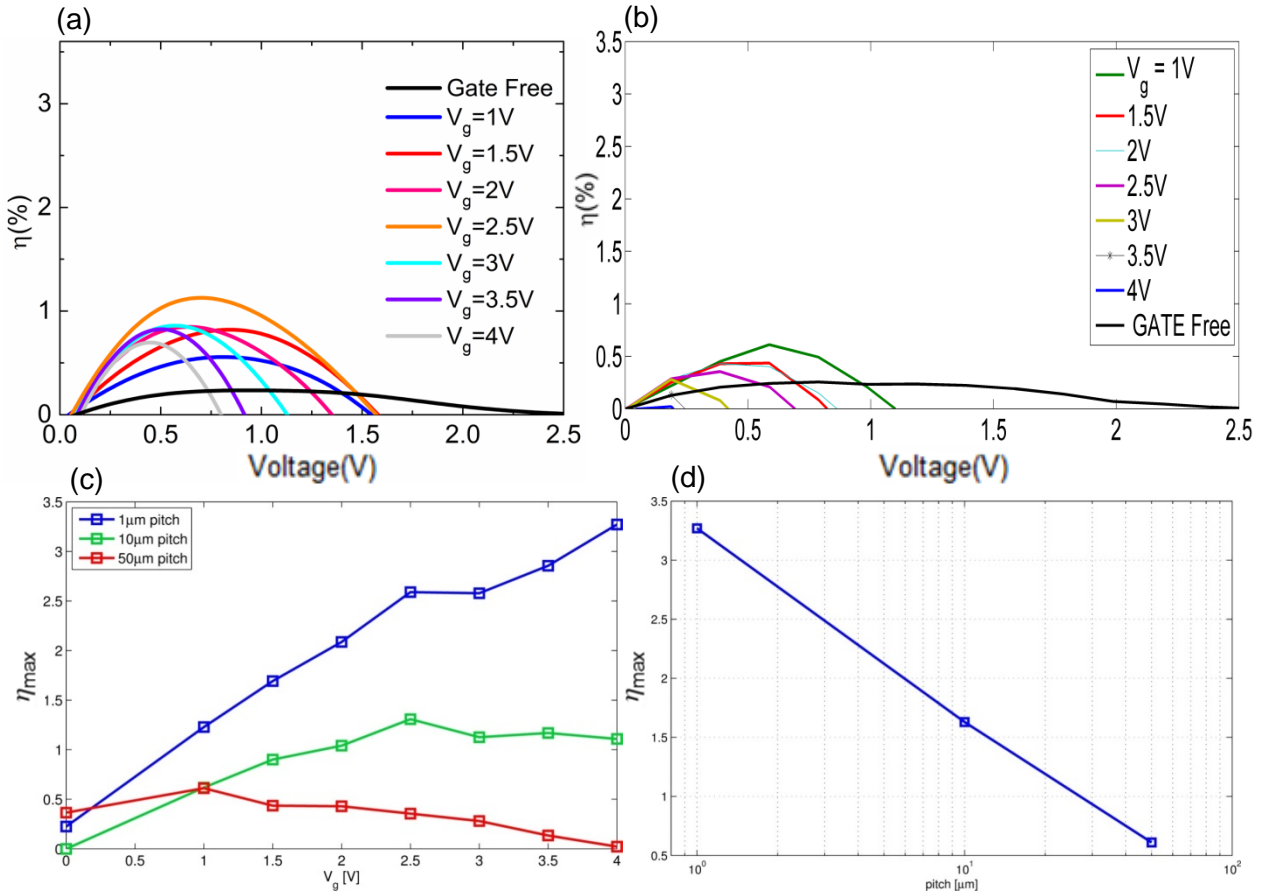


FIG. 5.4: (a) Power conversion efficiency  $\eta$  and operating voltage  $V$  as functions of the gate terminal voltage  $V_g$ . In this calculation the inter-electrode distance  $d_{ec}$  is  $20\ \mu\text{m}$ , pitch  $P$  is  $10\ \mu\text{m}$  and gate width  $G$  is  $P/10$ . (b) As in (a) but pitch  $P$  is  $50\ \mu\text{m}$ . (c) Maximum efficiency  $\eta_{\text{max}}$  as a function of the applied voltage  $V$  with respect to the pitch size. (d) Maximum efficiency as a function pitch size.

Note that when the pitch size increases the maximum efficiency of the device decreases. Also in (c) and (d) the inter-electrode gap is 20  $\mu\text{m}$ .

In particular, we have estimated the power conversion efficiency  $\eta$  for pitch sizes of 10  $\mu\text{m}$  and 50  $\mu\text{m}$ , while the width size of the gate terminal was kept constant at  $P/10$  and the inter-electrode distance was taken equal to 20  $\mu\text{m}$ , as shown in Fig. 5.4(a) and Fig. 5.4(b). By comparing  $P=1 \mu\text{m}$  (Fig. 5.3(b)),  $P=10 \mu\text{m}$  (Fig. 5.4(a)) and  $P=50 \mu\text{m}$  (Fig. 5.4(b)), we find that the maximum power conversion efficiency of a PETE device drops drastically upon pitch size increase (see Fig. 5.4(d)). A possible explanation lies in the weakening of the electric field produced by the gate upon pitch increase (the squared holes in the gate show bigger area). In fact, in case of 1  $\mu\text{m}$  pitch, we found that higher  $V_g$  the higher would have been the efficiency of the device, but this behaviour is not confirmed by  $P=10 \mu\text{m}$  and  $P=50 \mu\text{m}$  (see Fig. 5.4(c)). In particular, for  $P=10 \mu\text{m}$  the best performance is reached at  $V_g=2.5 \text{ V}$ , while for  $P=50 \mu\text{m}$  this happens at  $V_g=1 \text{ V}$ .

We have proposed a technique (gate insertion) to reduce the charge cloud effect in 3D-PETE devices while maintaining high distance between cathode and anode. This analysis is especially important from a feasibility point of view, inasmuch as greater  $d_{ec}$  translate in a easier and cheaper fabrication process. Finally, in the next section we are going to test our model when complex 3D structures are considered at the cathode side. Specifically, the cathode will be considered formed by an array of nano-cones with varying apex angle.

## 6. Nanostructured cathode study

The 3D COMSOL model here presented was applied only to flat cathodes and no tentative in describing more complicated surfaces was done. Here we shall consider nanostructured surfaces with the aim to increase the electron extraction efficiency from the surface itself.

The considered cathode surface is formed by an array of sharp nanocones. The idea behind this choice is to exploit a possible field enhanced emission at the cones apex. This is depicted in Fig. 6.1(a), (b). In presence of an applied anode potential an enhanced electrostatic field is produced at the tip apex. The extent of the field can be easily computed by solving the Poisson's equation. In the case reported in Fig. 6.1(a), a 500 nm pitch is set with a cone of 450 nm diameter and 100 nm height, while the tip curvature radius is 5 nm. Since the computational cost required to resolve the fine details of the cone tip is high, we considered only a relatively small anode-cathode distance, namely 2  $\mu\text{m}$ . A maximum field of  $8.5 \cdot 10^6 \text{ V/m}$  is predicted. As is reported in the schematic plot of Fig. 6.1(c), the extent of the surface is high enough to bend the electronic band structure at the cathode surface and to locally lower the work function required to extract electron to the continuum state (Fig. 6.1(d)). This phenomenon is commonly referred to as Schottky barrier reduction and is described by the following set of equations [40]:

$$\phi_{eff} = \phi_0 - \phi_{field}(x, y, z) \quad (32)$$

$$\phi_{field}(x, y, z) = \frac{e}{2} \sqrt{\frac{e |\mathbf{E}(x, y, z)|}{\pi \epsilon_0}} \quad (33)$$

$$J_s = J_{s,0} e^{\phi_{field}(x,y,z)/k_B T} \quad (34)$$

$$I = \int_{cathode} J_s d\sigma \quad (35)$$

In Eq. 32 the quantities  $\phi_{eff}$ ,  $\phi_0$ ,  $\phi_{field}$  are respectively the effective work function, the material work function in absence of electric field and the work function reduction due to the local electric field, at  $(x,y,z)$ . The latter is given by Eq. 33 as a function of the local electric field  $E(x,y,z)$ . The new saturation current density is given by Eq. 34. We notice that it is now space dependent. The total current emitted by the unitary cell is obtained by integration of  $J_s$  over the cathode surface, Eq. 35.

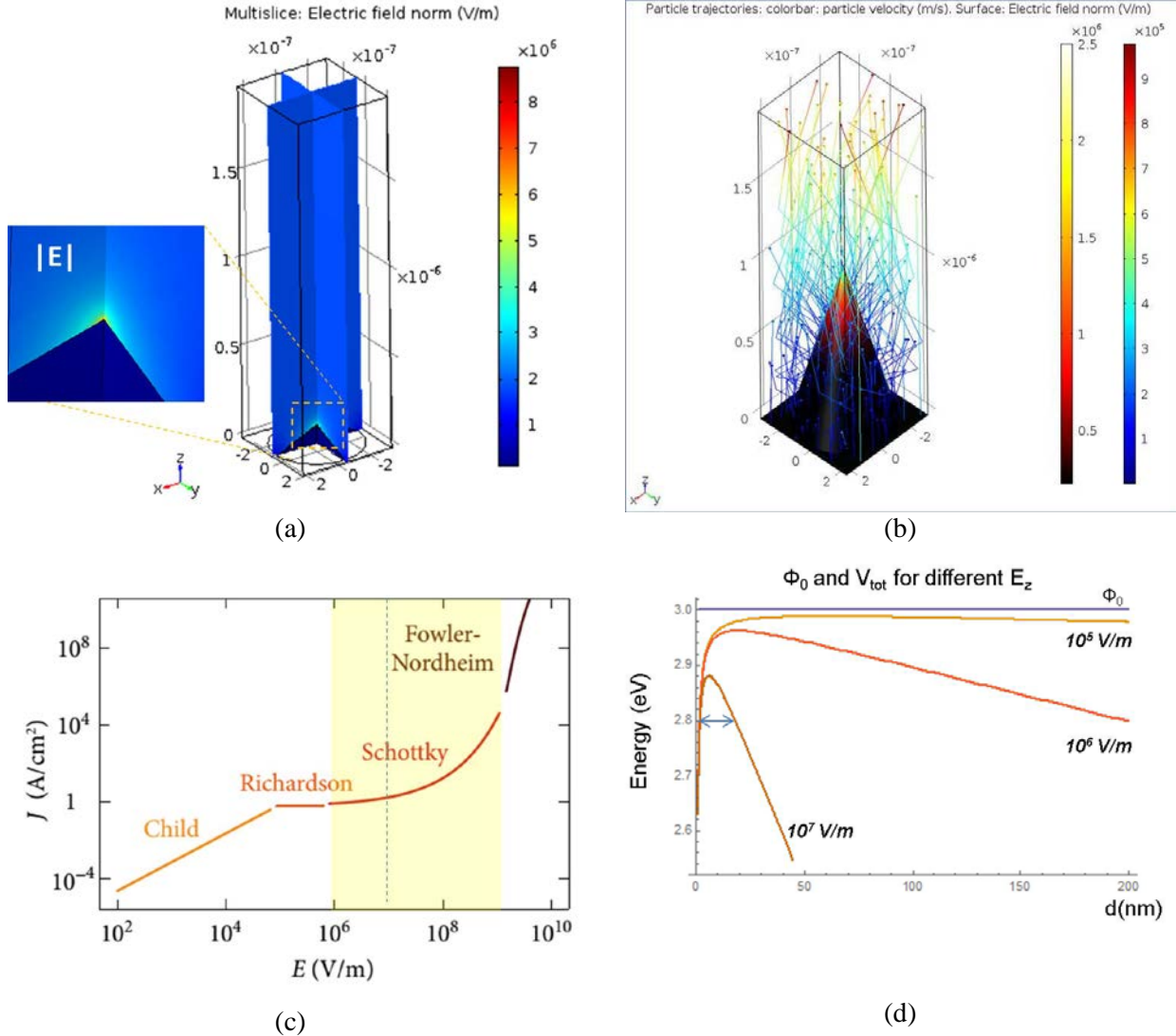


FIG. 6.1: (a) Example of the simulated nanostructured cone cathode emission model. The colour maps shows the electric field norm. Geometrical parameters are: Pitch = 500 nm, cone height = 100 nm, cone diameter = 450 nm, anode-cathode distance = 2  $\mu$ m, applied voltage = 1 V, temperature T = 800 K. (b) example of calculated electron trajectories. (c) Schematic plot of the different field induced electron emission as a function of the electric field at the surface. (d) Schematic plot of the surface barrier reduction for different applied electric fields.

The field enhanced current equations (32)-(35) have been implemented in COMSOL, and, in particular, the integrated current given by Eq. 35 has been set as an input to the inlet boundary conditions for the particle tracing simulation stage. In Fig. 6.2(a) we report the calculated J-V curves for different cone heights, keeping fixe cell period to 500 nm and curvature radius to 5 nm. It is clearly seen that, with respect to the flat cathode, an enhancement in current density is obtained for voltages lower than the saturation voltage, thanks to the field enhanced emission effect and to the increased emission surface. The maximum current enhancement is obtained for a cone height of about 50 nm. By further increasing the cone height a current drop is observed. The reason for this behaviour can be ascribed to the steeper cone slopes, which determines more electrons to be emitted at grazing directions and thus being more likely repelled back to the cathode by the space charge

induced potential. In Fig. 6.2(b) we report the corresponding PETE solar cell efficiencies. As is seen, in no case we obtain efficiencies higher than the case of flat anode.

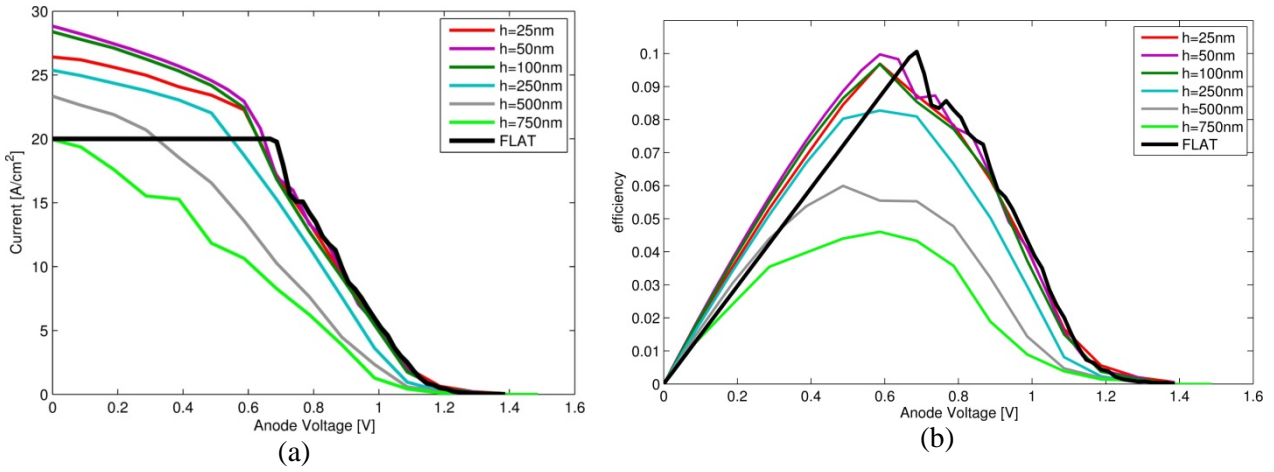


FIG. 6.2: J-V curves and (a) and efficiency curves (b) for a PETE based solar cell with nanostructured cone with pitch 500nm, anode-cathode distance 2µm, curvature radius of 5nm, for different cone heights. The black solid line represent the flat cathode case.

In Fig. 6.3(a), (b) we report respectively the field enhancement at the cone tip and the integral of the current density over the cathode surface as a function of the tip curvature radius, for different cone heights. It is clear that a little role is played by the tip curvature radius. As a matter of fact, on the one hand by reducing the radius a higher enhancement is expected at the tip apex, on the other hand the enhanced emission area is correspondingly reduced. The two effects counterbalance each other, resulting in a little variation of the overall integrated current as a function of the curvature radius.

In Fig. 6.3(c) we report several J-V for different periods of the unitary cell, keeping fixed the aspect ratio of the cone to 0.4, its diameter being 0.9 times the pitch of the cell. We notice that the emitting area exceeds that one of the flat cathode for the same amount for every pitch. As can be seen the JV curves only slightly differ from each other. This demonstrates that the contribution to the current enhancement with respect to the flat case is mainly due to the increase emitting area, while the field effect plays a little role. We can conclude therefore that the main beneficial effect of structuring the cathode derives from the increase of emission area.

Finally in Fig. 6.4(a), (b) we report the simulation of the combination of nanostructured cathode surface and gate insertion, in case of 1µm pitch and 20µm anode-cathode distance. The cone aspect ratio is set to 0.1, namely the value giving the best results in the study presented in Fig. 6.2. As is seen the best performance is obtained in case of cell without any cone but with gate. On the contrary the presence of the cone does not yield a real advantage.

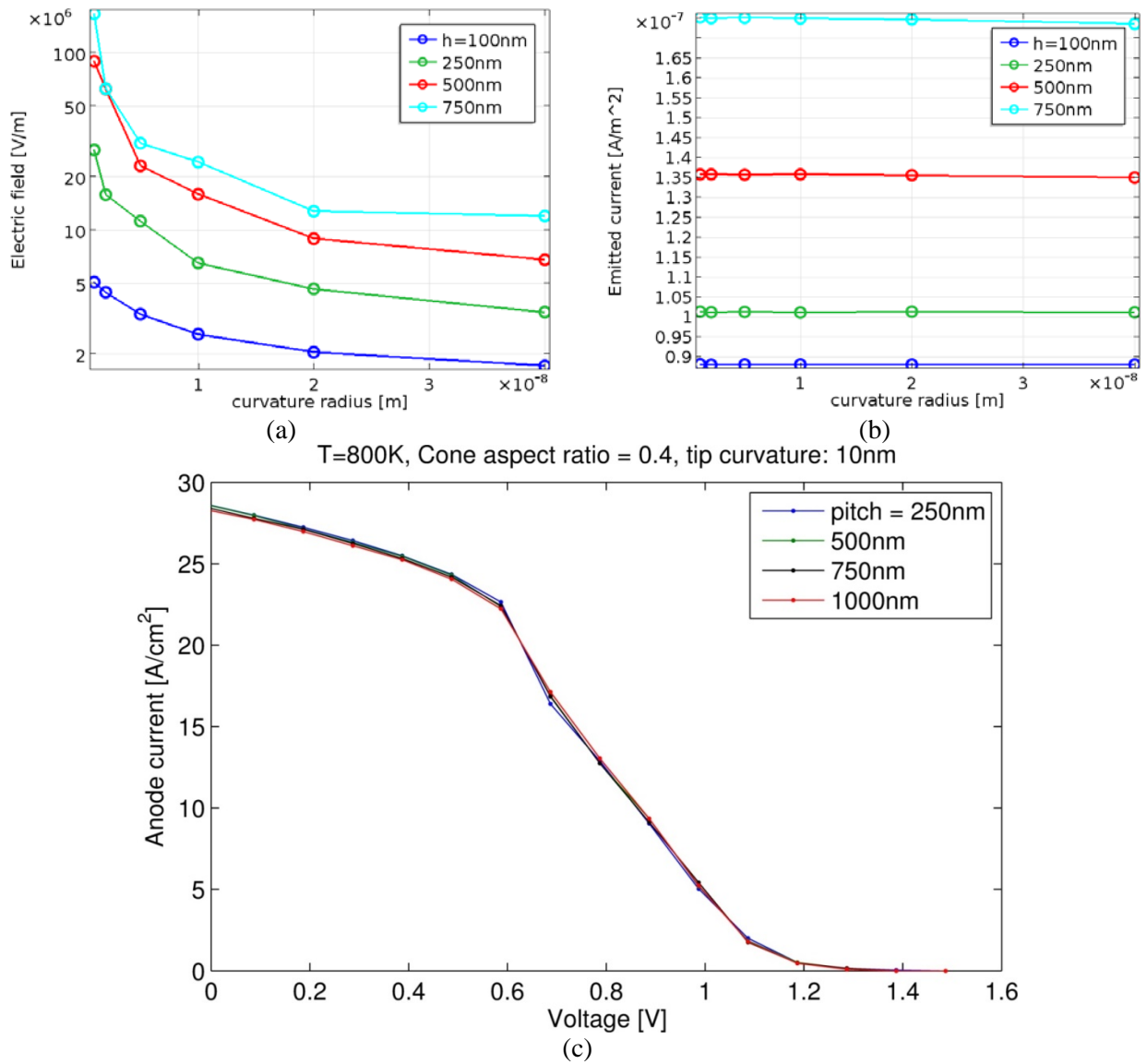


FIG. 6.3: (a) Electric field norm calculated at the tip of the cone whose parameters are listed in Fig. 5.2, for different cone heights as a function of the curvature radius at the tip. (b) Corresponding current emitted from the anode. (c) J-V curves calculated for a fixed cone aspect ratio of 0.4 and fixed diameter-to-pitch ratio of 0.9, for different cell pitches.

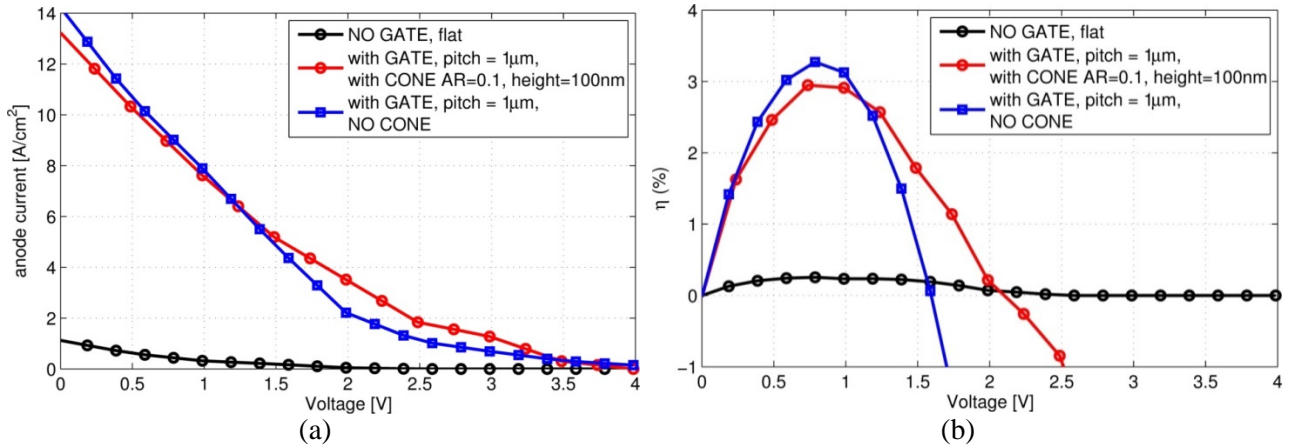


FIG. 6.4: J-V curves (a) and calculated efficiencies for PETE solar cells with  $20\ \mu\text{m}$  anode-cathode distance and flat anode with no gate (black), flat anode with gate (red), cone array anode and gate (blue). The pitch of both gate and cone array is  $1\ \mu\text{m}$ , gate wire width-to-period ratio is 0.9, cone aspect ratio is 0.1 (namely 100 nm height), diameter is 900 nm.

## CONCLUSION

In this work we have presented the Langmuir theory for 1D-TECs and its extension to describe 1D-PETE devices in order to estimate the influence of space charge cloud on the device power conversion efficiency  $\eta$ . From the 1D-PETE model we have concluded that at high current densities the performance of PETE solar cells will be negatively affected by the charge cloud produced in the vacuum gap between cathode and anode. It was found that by lowering the inter-electrode distance down to few microns, the detrimental effect due to the space charge cloud can be sensitively reduced. Due to fabrication constraint and with the idea of making a real power generation devices, we extended the 1D theory to a 3D system. We have also implemented a technique (gate insertion) to reduce the space-charge effect in 3D-PETE device while maintaining high cathode-anode distance. This was motivated by the fact that larger distances facilitate the fabrication process of the vacuum chamber between cathode and anode. Finally, in order to verify the capabilities of the simulation setup, we have implemented complex 3D structures for cathode by considering an array of nanocones with sharp apex. Interestingly, we found that the texturing of the cathode does not provide any advantage with respect to a flat surface. Finally, we would like to stress that the proposed numerical model can be used to design and implement any kind of electrode shape together with arbitrary gate devices.

## References

1. P.A. Iles, "Future of photovoltaics for space applications," *Prog. Photovoltaics Res. Appl.* 8 39–51 (2000).
2. J. Hall, D.A. Lamb, M.A. Baker, G. Kartopu, C.I. Underwood, R. Grilli, et al., "Lightweight and low-cost thin film photovoltaics for large area extra-terrestrial applications," *IET Renew. Power Gener.* 9 420–423 (2015).
3. D.M. Powell, M.T. Winkler, H.J. Choi, C.B. Simmons, D.B. Needleman, T. Buonassisi, "Crystalline silicon photovoltaics: a cost analysis framework for determining technology pathways to reach baseload electricity costs," *Energy Environ. Sci.* 5 5874 (2012).
4. C. Herring, M.H. Nichols, "Thermionic Emission," *Rev. Mod. Phys.* 21 185–270 (1949).
5. W.H. Preece, "On a Peculiar Behaviour of Glow-Lamps When Raised to High Incandescence," *Proc. R. Soc. London.* 38 219–230 (1884).
6. W. Schlichter, "Die spontane Elektronenemission glühender Metalle und das glühelektrische Element," *Ann. Phys.* 352 573–640 (1915).
7. G.N. Hatsopoulos, J. Kaye, "Measured Thermal Efficiencies of a Diode Configuration of a Thermo Electron Engine," *J. Appl. Phys.* 29 1124 (1958).
8. G.M. Grover, D.J. Roehling, E.W. Salmi, R.W. Pidd, "Properties of a Thermoelectric Cell," *J. Appl. Phys.* 29 1611 (1958).
9. M. Patel R., "Spacecraft Power Systems," CRC Press, United States, 2004.
10. V.C. Wilson, "Conversion of Heat to Electricity by Thermionic Emission," *J. Appl. Phys.* 30 475 (1959).
11. C. Stephanos, *Thermoelectronic Power Generation from Solar Radiation and Heat*, University of Augsburg, 2012.
12. J.-H. Lee, I. Bargatin, N.A. Melosh, R.T. Howe, "Optimal emitter-collector gap for thermionic energy converters," *Appl. Phys. Lett.* 100 173904 (2012).
13. Y.C. Gerstenmaier, G. Wachutka, Efficiency of Thermionic and Thermoelectric Converters, in: *AIP Conf. Proc.*, AIP, 2007: pp. 349–360.
14. V.V.S. Meir, *Highly-Efficient Thermoelectronic Conversion of Heat and Solar Radiation to Electric Power der Universität Augsburg*, n.d.
15. S. Meir, C. Stephanos, T.H. Geballe, J. Mannhart, "Highly-efficient thermoelectronic conversion of solar energy and heat into electric power," *J. Renew. Sustain. Energy.* 5 (2013).
16. S.F. Adams, *Solar Thermionic Space Power Technology Testing: A Historical Perspective*, in: *AIP Conf. Proc.*, AIP, 2006: pp. 590–597.
17. J.W. Schwede, I. Bargatin, D.C. Riley, B.E. Hardin, S.J. Rosenthal, Y. Sun, et al., "Photon-enhanced thermionic emission for solar concentrator systems.," *Nat. Mater.* 9 762–767 (2010).

18. G. Segev, Y. Rosenwaks, A. Kribus, "Limit of efficiency for photon-enhanced thermionic emission vs. photovoltaic and thermal conversion," *Sol. Energy Mater. Sol. Cells.* 140 464–476 (2015).
19. G. Segev, Y. Rosenwaks, A. Kribus, "Efficiency of photon enhanced thermionic emission solar converters," *Sol. Energy Mater. Sol. Cells.* 107 125–130 (2012).
20. J.W. Schwede, T. Sarmiento, V.K. Narasimhan, S.J. Rosenthal, D.C. Riley, F. Schmitt, et al., "Photon-enhanced thermionic emission from heterostructures with low interface recombination.," *Nat. Commun.* 4 1576 (2013).
21. G. Segev, A. Kribus, Y. Rosenwaks, "High performance isothermal photo-thermionic solar converters," *Sol. Energy Mater. Sol. Cells.* 113 114–123 (2013).
22. P. Iles, "Evolution of space solar cells," *Sol. Energy Mater. Sol. Cells.* 68 1–13 (2001).
23. S. Su, Y. Wang, T. Liu, G. Su, J. Chen, "Space charge effects on the maximum efficiency and parametric design of a photon-enhanced thermionic solar cell," *Sol. Energy Mater. Sol. Cells.* 121 137–143 (2014).
24. I. Langmuir, "The Effect of Space Charge and Initial Velocities on the Potential Distribution and Thermionic Current between Parallel Plane Electrodes," *Phys. Rev.* 21 419–435 (1923).
25. T. Ito, M.A. Cappelli, "Optically pumped cesium plasma neutralization of space charge in photon-enhanced thermionic energy converters," *Appl. Phys. Lett.* 101 213901 (2012).
26. G. Segev, D. Weisman, Y. Rosenwaks, A. Kribus, "Negative space charge effects in photon-enhanced thermionic emission solar converters," *Appl. Phys. Lett.* 107 013908 (2015).
27. Y.Y. Lau, "Simple Theory for the Two-Dimensional Child-Langmuir Law," *Phys. Rev. Lett.* 87 278301 (2001).
28. K.L. Jensen, "Space charge effects in field emission: Three dimensional theory," *J. Appl. Phys.* 107 014905 (2010).
29. G.N.H. E. P. Gyftopoulos, "Thermionic Energy Conversion, Vol. 1: Processes and Devices,," MIT Press, Cambridge, 1979.
30. T. Wang, J. Guo, J. Shao, D. Wang, A. Chen, M. Jin, "Ultrafast thermionic emission from metal irradiated using a femtosecond laser and an electric field in combination," *Phys. Plasmas.* 22 033106 (2015).
31. J.R. Smith, G.L. Bilbro, R.J. Nemanich, "Theory of space charge limited regime of thermionic energy converter with negative electron affinity emitter," *J. Vac. Sci. Technol. B Microelectron. Nanom. Struct.* 27 1132 (2009).
32. G.N.Hatsopoulos E.P.Gyftopoulos, "Thermionic Energy Conversion: Processes and Devices,," Cambridge, Massachusetts, 1973.
33. A.R. Knox, A. Asenov, A.C. Lowe, "An electron emission model for use with 3D electromagnetic finite element simulation," *Solid. State. Electron.* 45 841–851 (2001).
34. J. Buencuerpo, J.M. Llorens, P. Zilio, W. Raja, J. Cunha, A. Alabastri, et al., "Light-trapping in photon enhanced thermionic emitters," *Opt. Express* 23 A1220 (2015).

35. W. Tang, W. Yang, Y. Yang, C. Sun, Z. Cai, "GaAs film for photon-enhanced thermionic emission solar harvesters," *Mater. Sci. Semicond. Process.* 25 143–147 (2014).
36. J.C. Mudiganti, *An Emission Model for the Particle-in-Cell*, Thesis, <http://tuprints.ulb.tu-darmstadt.de/887/1/Mudiganti.pdf>, 2006 .
37. S. Humphries, "Cathode thermal effects in one-dimensional space-charge-limited electron flow," (2012).
38. S. Meir, C. Stephanos, T.H. Geballe, J. Mannhart, "Highly-efficient thermoelectronic conversion of solar energy and heat into electric power," *J. Renew. Sustain. Energy.* 5 (2013).
39. "Solar Spectral Irradiance: ASTM G-173," (n.d.)  
<http://rredc.nrel.gov/solar/spectra/am1.5/astmg173/astmg173.html> .
40. S.M. Sze, C.R. Crowell, D. Kahng, "Photoelectric Determination of the Image Force Dielectric Constant For Hot Electrons in Schottky Barriers," *J. Appl. Phys.* 35 2534 (1964).